INVERSE DESIGN AND OPTIMIZATION METHODS FOR THERMOPHOTOVOLTAIC EMITTERS MADE OF TUNGSTEN GRATINGS

A Thesis
Presented to
The Academic Faculty

By

Preston R. Bohm

In Partial Fulfillment
of the Requirements for the Degree
Master of Science in the
School of Mechanical Engineering
College of Engineering

Georgia Institute of Technology

December 2022

INVERSE DESIGN AND OPTIMIZATION METHODS FOR THERMOPHOTOVOLTAIC EMITTERS MADE OF TUNGSTEN GRATINGS

Thesis committee:

Dr. Zhuomin Zhang, Advisor
Mechanical Engineering
Georgia Institute of Technology

Dr. Peter J. Hesketh
Mechanical Engineering
Georgia Institute of Technology

Dr. Akanksha Menon
Mechanical Engineering
Georgia Institute of Technology

Date approved: December 8th, 2022

ACKNOWLEDGMENTS

I would like to thank my mentor and advisor, Professor Zhuomin Zhang, for teaching me how to be a good researcher and providing me with his guidance and expertise throughout my undergraduate and graduate education. I would also like to thank my committee members, Professor Akanksha Menon and Professor Peter J. Hesketh, for their contributions to the evaluation of this Thesis. The current and former members of the Nanoscale Thermal Radiation Group have made this thesis possible, particularly Chiyu Yang.

Professor Bernard Kippelen equated my graduate education to climbing a mountain, it is this analogy and his advice that keeps me motivated to this day. Additionally, the Department of Energy made this thesis possible with their continued support of this work.

My parents and family have been the most important part of this journey; they have been teaching me for roughly 24 years. I hope to one day have my father's work ethic, be half the researcher my mother is, and have a quarter of my sister's compassion. It is them that always have my back in whatever I need.

TABLE OF CONTENTS

LIST OF TABLES

LIST OF FIGURES

LIST OF ACRONYMS

CNN Convolutional Neural Network

CUDA Compute Unified Device Architecture

DE Differential Evolution

FA Firefly Algorithm

FCNN Fully Connected Neural Net

FDTD Finite-difference time-domain

GA Genetic Algorithm

GPU Graphical Processing Unit

HH Hyper-Heuristics

LReLU Leaky Rectified Linear Unit

LSTM Long short-term memory

MH Metaheuristics

PSO Particle Swarm Optimization

RCWA Rigorous coupled-wave analysis

ReLU Rectified Linear Unit

RNN Recurrent Neural Network

RS Random Search

TE Transverse Electric

TM Transverse Magnetic

TPV Thermophotovoltaics

LIST OF SYMBOLS

Latin Symbols

A	Absorptance
a	Activation function
b	Bias for neural net
$\mathbb{C}$	Complex numbers
c	Speed of light in a medium
c_0	Speed of light in a vacuum
$\mathscr{E}$	Electric field
E_i	Intrinsic fermi level
E_p	Energy of phonon assistance
E_{Fn}	Fermi level energy in a N type semiconductor
E_{Fp}	Fermi level energy in a P type semiconductor
E_c	Minimum energy of the conduction band
E_v	Minimum energy of the valence band
e	Elementary charge
D	Problem dimension
$D_{e,h}$	Diffusion coefficient for electrons or holes
d	Depth of grating
DE	Diffraction efficiency
f	Filling factor of grating
g'	Rate of generation of new carriers

H	Heavy-side function
$\mathscr{H}$	Magnetic field
h	Planck constant
$\hbar$	Reduced Planck constant
i	Imaginary unit $\sqrt{-1}$
J	Current
k	Wave vector
k_b	Boltzmann constant
$L_{e,h}$	Diffusion length for electrons or holes
N	Diffraction orders
N_A	Number density of accpetors
N_D	Number density of doners
N_i	Number density of intrinsic carriers
$\mathbb{N}$	Natural numbers
n	Electron concentration or population index
n_i	Intrinsic carrier concentration
n_{index}	Index of refraction
p	Hole concentration
P_E	Maximum power
q"	Energy flux
R	Reflectance
$R_D(\theta)$	Rotation matrix
$\mathbb{R}$	Real numbers
$\mathfrak{S}$	Set of all solutions
$\boldsymbol{s}$	Solution
$\boldsymbol{s}^*$	Best solution

T Temperature

T_m Transmittance

t Algorithm iteration

$t_{e,h0}$ Minority carrier lifetime under low injection

$U(x, y)$ Uniform random number of the set (x,y)

V Voltage

Greek Symbols

α Absorption coefficient

γ Space harmonic of electric field

ϵ Emittance

ϵ' Real part of the dielectric function

ϵ" Complex part of the dielectric function

ϵ_0 Vacuum permittivity

ϵ_r Relative permittivity

η Efficiency

$\Theta(\omega, T)$ Mean energy of Planck's oscillator

θ Zenith angle

Λ Period of a grating

$\mu_{e,h}$ Mobility of electrons and holes

μ_0 Permeability of vacuum

μ_r Relative permeability

χ Space harmonic of electric field

$\rho_c(\omega)$ Density of states

$\tau_{e,h}$ Relaxation time for electrons or holes

ϕ Azimuthal angle

ψ Polarization angle

ω Angular frequency

Other Symbols

$\forall$ For All

$\odot$ Hadamard-Schur Product

SUMMARY

Periodic gratings utilized as emitters increase the efficiency of thermophotovoltaic (TPV) systems. These gratings work by altering the emittance spectrum incident on the photovoltaic cell to better match the band gap of the cell. Photons at slightly higher energies than the band gap are the most efficient as they generate electron-hole pairs while minimizing thermalization losses. This prompts the use of gratings to be used as selective emitters. Even for a one-dimensional (1D) grating, millions of possible geometries exist, and simulating even a fraction is infeasible. This prompts the use of metaheuristics. It should be noted that due to the stochastic nature of these optimization methods, a globally optimal solution is not guaranteed, and instead, these methods seek to provide "close enough" solutions.

Generally, metaheuristic algorithms have been extensively studied and compared with each other; according to the "no free lunch" (NFL) theorem, all optimization algorithms are equivalent when averaged over all possible problems. Therefore, a comparison of existing algorithms for the optimization of a system, composed of a 2,000 K 1D tungsten binary grating paired with a 300 K InGaSb cell, was performed. After using the comparison, a hyper-heuristic optimization was used to algorithmically develop a purpose-built metaheuristic algorithm. Rigorous coupled-wave analyses (RCWA) take too long to natively perform for the hyper-heuristic search. Fully connected neural nets (FCNN) solve this problem when used as surrogate models. The new optimization algorithm created in this way showed significantly better performance than all the existing algorithms it was compared against. Then, this algorithm was used to optimize emitters for a normalized emittance spectrum, maximum efficiency, and maximum power.

CHAPTER 1
INTRODUCTION

Heat Transfer is of foundational importance to a broad range of engineering applications. Radiation heat transfer, that is the transfer of energy through electromagnetic waves/photons, is the most universal, as it needs no facilitating medium [1][2]. This results in greater distances being impacted compared to convection or conduction. Radiative heat transfer also dominates at higher temperatures. This makes it incredibly important for aerospace and naval applications. Micro/Nanostructures and metamaterials allow for unprecedented control of the optical properties that drive the radiative heat transfer effects.

Optical nanostructures and Metamaterials can achieve optical responses not possible with natural bulk materials, through the use of arranged structures with dimensions smaller than the wavelengths of interest. The sub-wavelength nature of these structures insure that the optical properties of the material is not predominately determined by bulk optical phenomena, as would be the case with wavelength scale structures [3].

Metamaterials and Micro/Nanostructures have a broad range of novel applications. Famously, metamaterials have been used to simultaneously exhibit negative permeability and permittivity [4][5]. Micro/nanostructures, particularly one-dimensional gratings can be used to optimize thermophotovoltaic (TPV) emitters to better match the band gap energy of the photovoltaic cell [6][7]. Metamaterials have also been implemented to create super lenses that can overcome the diffraction limit associated with geometric optics [8]. Research has also shown their feasibility for cloaking applications [9]. Circular and Linear polarization effects can also

be manipulated with metamaterials, having beneficial applications to Stereochemistry[10][11][12].

Due to the wide range of applications for optical nano-structures and their infinite possible complexity, it can be challenging to determine new designs and geometric parameters for new applications or to further optimize existing applications. This presents several unique problems in understanding the complex non-linear phenomena that drive different architectures. This study primarily investigates a small subset of optical nano-materials known as diffraction gratings, particularly those made of Tungsten. The optimization methods associated with the discovery of new grating configurations will be explored in this study, and how tungsten gratings can be used in TPV systems.

The fundamentals of the photoelectric effect is first introduced along with its utilization in semiconductors and photo-diodes is first introduced. Along with the purpose of emitters in TPV systems. From there, a background on calculating the optical properties of gratings with RCWA is shown, including the special considerations needed for conical diffraction scenarios. Then, an explanation of the basic fundamentals of Neural Networks is provided to facilitate an understanding of their utilization in subsequent sections.

An overview of existing optimization algorithms and how they can be broken down into building blocks is provided. This building block model of algorithms allows for the rearrangement of building blocks to create new algorithms through Hyper-heuristic optimization techniques. Then these new algorithms are compared to existing optimization algorithms. These Hyper-heuristic techniques are made possible with the implementation of RCWA surrogate neural net models, which increase the calculation time of optical properties by several orders of magnitude, at the cost of initial training data.

A model was developed to calculate the efficiency at maximum power for a particularly TPV system. This model assumed 100% internal quantum efficiency. The aforementioned optimization methods were implemented to produce gratings optimized to have maximum power and efficiency. The optical properties of these gratings were investigated to allow for conclusions of which particular behaviors are of particular interest to TPV systems. Overall, this study aims to advance the design and optimization of one-dimensional gratings for any application and uses TPV systems as a robust real-world example.

CHAPTER 2
THEORETICAL BACKGROUND AND PROBLEM

2.1 Thermophotovoltaics

The defining characteristic of humankind's success in the last 500 years has been the ability to "trick" energy, particularly heat, into doing work. This first started with ancient water mills and steam engines, like Hero's Aeolipile [13], and evolved into the complex hydroelectric dams and steam engines that supply the world's electricity today. Thermophotovoltaics (TPV) similarly "tricks" heat, photons radiating from a heated thermal body are converted directly into electricity without the need for working fluids or moving parts. This is accomplished through the photovoltaic effect, first demonstrated by Edmond Becquerel in 1839 [14].

2.1.1 Photovoltaic Effect in Semiconductors

The photovoltaic effect is the transfer of a photon's energy to an electron, which promotes the electron to a higher energy orbital. Ideally, this promotion would be from the valence band to the conduction band of the atom. This creates and electron-hole pair. The electron and hole can still have an inherent electric attraction to one another, meaning promotion can happen but the electron will still be bonded to the hole. This is referred to as the optical bandgap [15]. The amount of energy required for promotion and to sever inherent bonding is called the electronic bandgap. The electronic bandgap is of primary interest for photovoltaic power generation.

However, this promotion of electrons is not always a straightforward jump. The minimum energy of the conduction band does not always line up with the maximum energy of the valence band at the same k value. When these k values align, this is

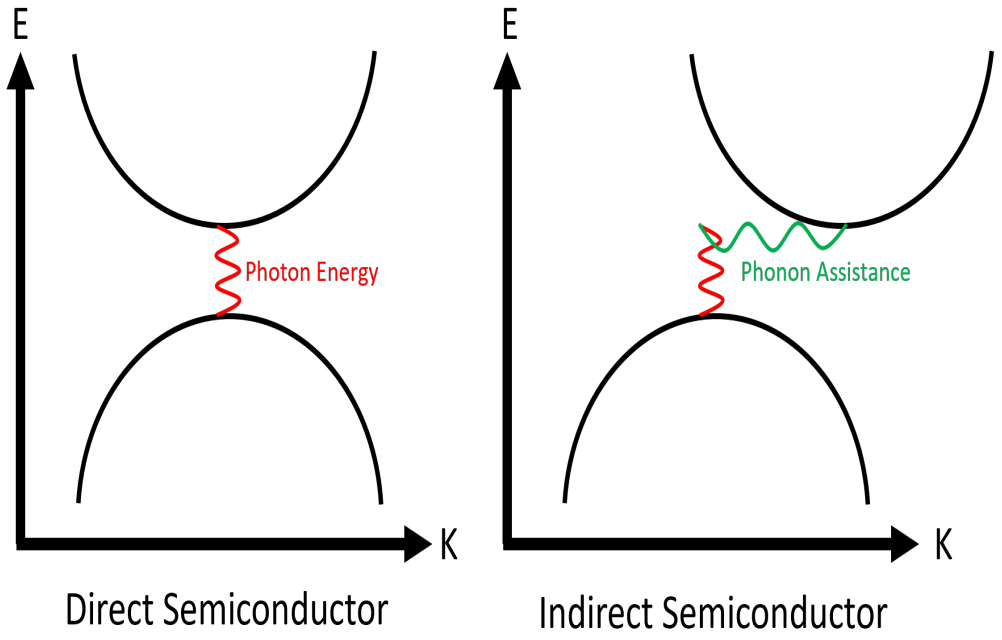

Figure 2.1: Direct vs. Indirect Bandgap Semiconductors

known as a direct bandgap material. Reciprocally, a misalignment of these k values is called an indirect bandgap material[16]. Figure 2.1 depicts a simplified diagram of the differences. This behavior is driven by the chemistry of the atoms and the crystalline structure of the material. For instance, crystalline Silicon is an indirect material while amorphous Silicon is direct material. In both types of materials, momentum must always be conserved with electron promotion, therefore a transition in an indirect bandgap material must be facilitated by an interaction with the crystal in the form of a phonon[16], this is represented depicted in Figure 2.1. The nature of the band gap also affects the absorption coefficient. At frequencies slightly higher than the direct bandgap the absorption coefficient is related by [17]:

$$\alpha \propto \frac{\pi e^2 x_{vc}^2 \omega}{\epsilon_0 \hbar n_{\text{index}} c} \rho_c(\omega)[f_v(\hbar\omega) - f_c(\hbar\omega)] \tag{2.1}$$

where $f_v(\hbar\omega)$ and $f_c(\hbar\omega)$ are the Fermi-Dirac functions:

$$f_v(\hbar\omega) = \frac{1}{1 + \exp([E_v(\hbar\omega) - E_{fp}]/k_bT)}$$

$$f_c(\hbar\omega) = \frac{1}{1 + \exp([E_c(\hbar\omega) - E_{fn}]/k_bT)}$$

and x_{vc} is a matrix element dependent on the crystal structure, E_v and E_c are the valence and conduction band energy levels, $\hbar$ is Plank's constant, k_b is Boltzmann's constant, T is the temperature, ϵ_0 is the permittivity of free space, c is the speed of light, ω is the frequency, n_{index} is the index of refraction, and e is the elementary charge. The Fermi Dirac functions represent the probability that a state at a certain energy level will be occupied. In indirect bandgap materials, the absorption coefficient during electron promotion is related by[18] :

$$\alpha \propto \frac{(\hbar\omega - E_c - E_v + E_p)^2}{exp(E_p/(k_bT)) - 1} + \frac{(\hbar\omega - E_c - E_v - E_p)^2}{1 - exp(-E_p/(k_bT))} \tag{2.2}$$

where E_p is the energy from the phonon assistance.

The photovoltaic effect can happen in any type of atom. However, it is most useful when occurring in semiconductors. In insulators, most photons do not carry the energy required to promote electrons across large band gaps. In conductors, the conduction band and valence band overlap with each other causing free elections to always be available. The movement of these electrons is (mostly) random, resulting in (almost) no current flow. Semiconductors on the other hand do not have overlapping conduction and valence bands; yet, the bandgap involves reasonable photon energies. Additionally, to further facilitate current flow, semiconductors take advantage of diodes (p-n junctions) to force the flow of electrons in 1 direction.

These p-n junctions are composed of p-type and n-type semiconductors metallurgically fused together. P-type semiconductors are doped with atoms with fewer

Table 2.1: Bandgaps of a Variety of Semiconductors at Room Temperature (300K)

Symbol	Name	Group	Type	Bandgap [eV]	Reference
Si	Silicon	IV	Indirect	1.14	[19]
Ge	Germanium	IV	Direct	0.67	[19]
GaSb	Gallium antimonide	III-V	Direct	1.43	[20]
InSb	Indium antimonide	III-V	Direct	0.17	[20]
AlP	Aluminium phosphide	III-V	Indirect	2.5	[19]
CdTe	Cadmium telluride	II-VI	Direct	1.5	[21]
Cd_3P_2	Cadmium phosphide	II-V	Direct	0.55	[22]
$\beta - CuGaO_2$	Copper Gallium Dioxide	I-III-VI_2	Direct	1.47	[23][24]

electrons in their valence shell than the valency properties of the intrinsic semiconductor, resulting in a net positive charge. Common atoms for this doping are Boron, Zinc, Cadmium, and Beryllium. N-type semiconductors are instead doped with atoms with more electrons in their valence shell than the valency of the intrinsic semiconductor, typically: Phosphorous, Arsenic, Antimony, and Selenium.

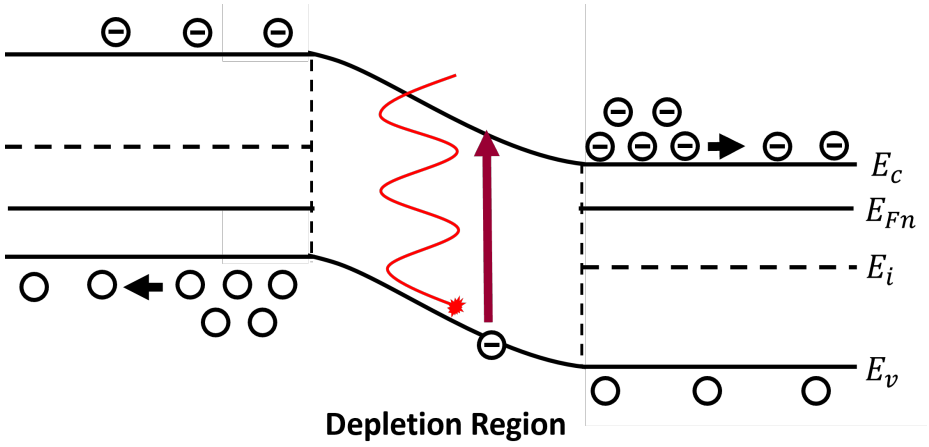

Figure 2.2: Zero Bias P-N Junction

Figure 2.2 shows a band diagram of a P-N junction under equilibrium, assuming both the P and N doped semiconductors are non-degenerate. The difference in conduction band energy levels creates a "hill" for electrons in the n-region, except instead of gravity creating the barrier it is created by an electric field. This electric

field is related to the charge density with Poisson's equations:

$$\nabla \cdot \mathscr{E} = \frac{\rho_c}{\epsilon_r \epsilon_0} \tag{2.3}$$

which, can be simplified to fit a 1 dimensional model of a P-N junction:

$$\frac{d\mathscr{E}}{dx} = \frac{\rho_c}{\epsilon_r \epsilon_0} \tag{2.4}$$

where ρ_c is the density of carriers, and ϵ_r is the relative permittivity. The size of this "hill" is quantized in the form of an unbiased or built-in voltage, related to the number of charge carriers:

$$V_{\text{built in}} = \frac{k_b T}{e} \ln\left(\frac{N_A N_D}{n_i^2}\right) \tag{2.5}$$

where N_A and N_D are the number of acceptor and donor carriers and n_i is the number of intrinsic carriers. There is an equivalent barrier or "hill" to holes in the p-region since they have negative effective mass. This electric field causes carriers to Drift in accordance with Ohm's law, $J_{\text{drift}} = e\rho_c \mu_{e,h} \mathscr{E}$, where $\mu_{e,h}$ is the mobility of electrons and holes respectively. The mobility of electrons due to this effect is referred to as the drift current J_{drift}. The number of carriers can be determined in a P-N junction at equilibrium with [16]:

$$N_D = n = n_i \exp\left(\frac{E_f - E_i}{k_b T}\right) \tag{2.6}$$

and for acceptors:

$$N_A = p = n_i \exp\left(\frac{E_i - E_f}{k_b T}\right) \tag{2.7}$$

Therefore, it is obvious that the p-region is going to have more holes than the n-

region, and reciprocally the n-region is going to have more electrons than the p-region. This causes diffusion of carriers in accordance with Fick's law, $J_{\text{diffusion}} = -eD_{e,h}\frac{d\rho_c}{dx}$. These movements of carriers cause a significant unbalanced dopant site charge near the metallurgical junction. This region around the junction where there is a non-zero charge is referred to as the depletion region, as a reference to the apparent depletion of charge carriers. The relationship of diffusion and drift current can be related to the ambipolar transport equation [16]. For p-type semiconductors:

$$D_e\frac{\partial^2(\partial n)}{\partial x^2} + \mu_n\mathscr{E}\frac{\partial(\partial n)}{\partial x} + g' - \frac{\partial n}{t_{e0}} = \frac{\partial(\partial n)}{dt} \tag{2.8}$$

where (∂n) is the excess minority carrier, electron concentration and t_{e0} is the minority carrier lifetime under low injection. g' is the generation of new carriers, this will be visited later.

Equivalently for n-type semiconductors:

$$D_h\frac{\partial^2(\partial p)}{\partial x^2} + \mu_p\mathscr{E}\frac{\partial(\partial p)}{\partial x} + g' - \frac{\partial p}{t_{h0}} = \frac{\partial(\partial p)}{dt} \tag{2.9}$$

where (∂n) is the excess minority carrier, hole concentration, and t_{h0} is the minority carrier lifetime under low injection. $D_{e,h}$ represents the diffusion coefficient for electrons and holes.

However, it is advantageous to change the size of the hill for photovoltaic purposes. Here a forward bias is applied to the P-N junction to reduce the size of the "hill". This causes an increase in the supply of majority carriers, resulting in an increase in the diffusion current. The drift current remains the same as the supply of minority carriers is constant with the applied bias. It is worth noting that the number of carriers with sufficient energy to overcome the "hill" increases exponentially with the applied bias V_A[16].

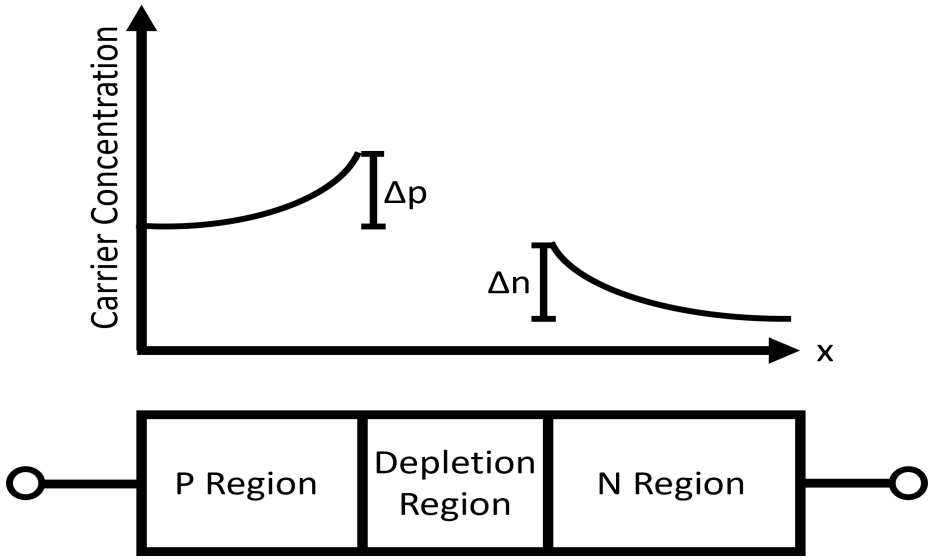

Figure 2.3: Carrier Concentration in a Forward Biased P-N Junction

Under bias, the P-N junction is no longer under equilibrium conditions. However, the electric field outside of the depletion region is assumed to be zero $\mathscr{E} \approx 0$, in so-called quasi-neutral regions. The carrier concentrations in these regions can be found with:

$$n = n_i \exp(\frac{E_{fn} - E_i}{k_b T}) \tag{2.10}$$

$$p = n_i \exp(\frac{E_i - E_{fp}}{k_b T}) \tag{2.11}$$

Then the current flow from electron and hole carrier gradients in each quasi-neutral region can be found with[25]:

$$J_h(x) = -eD_h \frac{d\Delta p}{dx} = \frac{eD_h}{L_h} \Delta p \exp(-x/L_h) \tag{2.12}$$

$$J_e(x) = -eD_e \frac{d\Delta n}{dx} = \frac{eD_e}{L_e} \Delta n \exp(-x/L_e) \tag{2.13}$$

where $L_{e,h}$ is the minority carrier diffusion length for electrons and holes respectively.

These properties are related to the relaxation time $\tau_{e,h}$ with the following relation:

$$L_{e,h} = \sqrt{D_{e,h}\tau_{e,h}} \tag{2.14}$$

The current flow in each quasi-neutral region can be used as boundary conditions to solve the dark current of the diode with no carrier generation[16]:

$$\overrightarrow{J}_{\text{dark}} = \overrightarrow{J}_{\text{Diffusion}} + \overrightarrow{J}_{\text{drift}} \tag{2.15}$$

$$\overrightarrow{J}_{\text{dark}} = J_0(\exp(\frac{eV}{k_bT} - 1)) \tag{2.16}$$

where:

$$J_0 \approx J_{\text{Diffusion}} = e((\frac{N_i^2}{N_A}\sqrt{\frac{D_e}{\tau_e}}) + (\frac{N_i^2}{N_D}\sqrt{\frac{D_h}{\tau_h}})) \tag{2.17}$$

Whenever a semiconductor is in non-thermal equilibrium, recombination and generation processes aim to bring balance to the energy carriers in the device. These effects include band-to-band recombination and generation, R-G center recombination and generation, auger recombination, and generation via impact ionization [25]. The focus of this study is not on optimizing these generation processes, therefore 100% internal quantum efficiency will be assumed to determine the current generation from incident photons, J_{ph}. This means every photon is assumed to generate 1 electron-hole pair in the depletion region of the P-N junction. The current flow from incident photons is determined with:

$$\overrightarrow{J}_{ph} = \int_{\omega_g}^{\infty} \frac{e}{h\omega} q"(\omega) d\omega \tag{2.18}$$

The total current flow is the combination of photocurrent and dark current.

$$\overrightarrow{J}(V) = \overrightarrow{J}_{ph} + \overrightarrow{J}_{\text{dark}}(V) \tag{2.19}$$

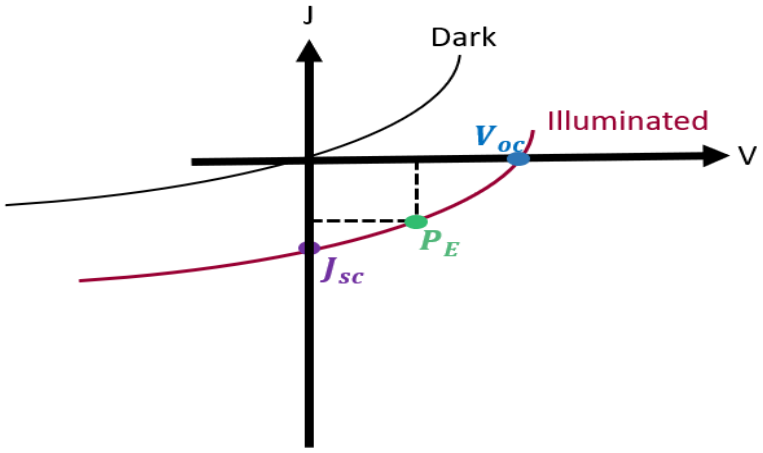

Figure 2.4: J-V Characteristics of a Diode

Figure 2.4 shows the current density and voltage characteristics of a diode in at equilibrium and a diode being illuminated. Here J_{sc} is equivalent to J_{ph} since the photocurrent is the only mechanism contributing to non-equilibrium in our model. V_{oc} is the voltage of the diode with no current flow[26]:

$$V_{oc} = \frac{k_b T}{e} \ln(J_{ph}/J_s + 1) \tag{2.20}$$

where $J_s = J_0$ is assumed. The power, $P = \overrightarrow{J} \cdot V$, of the PV cell depends on the operating voltage. The maximum power that a PV cell is capable of generating can be determined with the illuminated diode curve as seen in Figure 2.4. The maximum power generated is[26]:

$$P_E = J_{ph} V_{oc} [1 - \frac{1}{\ln(J_{ph}/J_s)}][1 - \frac{\ln(\ln(J_{ph}/J_s))}{\ln(J_{ph}/J_s)}] \tag{2.21}$$

2.1.2 Emitters

Instead of the incident photons on a photovoltaic cell coming directly from the sun or another light source as seen with solar photovoltaics, thermophotovoltaics pair low bandgap photovoltaic cells with emitters. These emitters absorb heat and re-emit the energy as photons at desirable frequencies onto the cell. The source of heat can come from a myriad of sources, such as waste heat from power plants, radioactive isotopes[27], sun [28], and waste heat from spacecraft [29]. This flexibility combined with the absence of moving parts is the primary advantage of TPV systems [30].

Generally, the optical performance of an emitter is determined by the ability to selectively radiate energy in a specific wavelength region. This wavelength region is usually at energies just above the bandgap of the PV cell, as energies below the bandgap have a low probability of creating electron-hole pairs, and energies much larger than the bandgap have energy lost to thermalization. Due to the large operating temperatures of TPV systems, emitters must also exhibit long-term high-temperature stability. There are a plethora of emitter materials and structures to try to optimize these metrics for different system implementations [31].

Tungsten, W, has been extensively identified as a suitable material for TPV applications[32, 33, 34], this is due Tungsten's chemical stability and high melting temperature of around 3600K [35]. The desirable thermal properties of Tungsten have been combined with different structures such as thin multilayer films[36], photonic crystals[36] and diffraction gratings [33]. These structures work to enhance the optical properties with sub-wavelength geometric features. The baseline optical properties of Tungsten are presented by Palik [37]. The primary type of emitters explored in this document are 1-dimensional gratings made of Tungsten deposited on a Tungsten substrate.

2.2 Diffraction Gratings

One-dimensional gratings have the advantage of being relatively easier to manufacture than some of the more complicated proposed structures for selective emitters. Their simplicity also comes with the advantage of being able to be represented with few parameters. Figure 2.5 shows how a periodic grating can be represented with as few as 3 parameters, Λ, w, d.

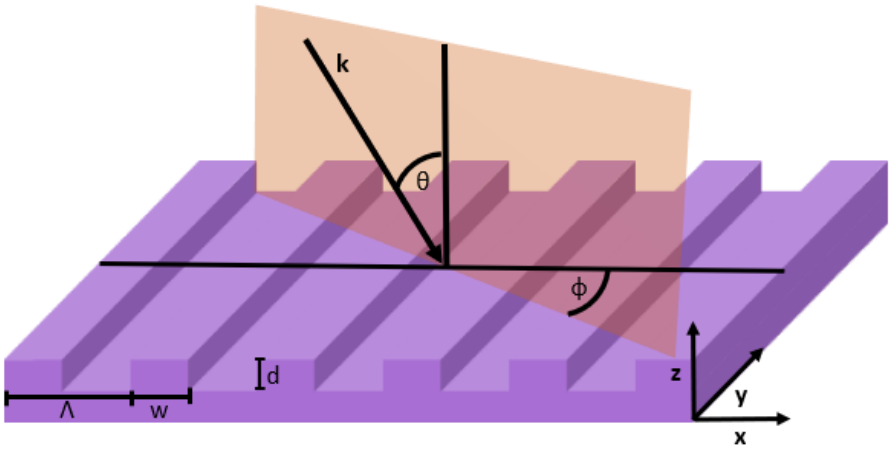

Figure 2.5: Periodic Binary Grating

These gratings fundamentally work based on the Huygen-Fresnel principle, which states that every point on a wavefront is itself the source of spherical wavelets, and the secondary wavelets emanating from different points mutually interfere with each other. These micro/nano structures also take advantage of several optical phenomena (e.g. surface plasmon polaritons (SPPs), microcavity resonance, magnetic polaritons (MPs) and inter-resonance interactions) to exhibit their selective emitter characteristics.

2.3 Rigorous coupled-wave analysis

Due to the complex non-homogeneous nature of Maxwell's equations in 1D grating, several different computational methods have been utilized to handle computing the optical properties: Finite Difference Time Domain (FDTD) [38], effective medium theory [39] and rigorous coupled-wave analysis (RCWA) [40, 41]. All of these methods have various advantages and disadvantages for their utility on calculating the optical properties of sub-wavelength structures. However, analysis in frequency domain with rigorous coupled-wave analysis calculates the optical properties of 1-dimensional periodic structures much faster by taking advantage of Floquet's theorem.

Floquet's theorem generally states that if there is a system of linear differential equations:

$$\frac{dx(t)}{dt} = \boldsymbol{A}(t)x(t) \tag{2.22}$$

and $\boldsymbol{A}(t)$ is a real, non singular, periodic $n \times n$ matrix such that:

$$\boldsymbol{A}(t+T) = \boldsymbol{A}(t)$$

where t, T are arbitrary parameters the function is periodic in (time, space, etc). This system must have the fundamental matrix solution $\boldsymbol{P}$, of the form:

$$\boldsymbol{P}(t+T) = \boldsymbol{P}(t)\boldsymbol{P}^{-1}(0)\boldsymbol{P}(T) \tag{2.23}$$

The monodromy matrix $\boldsymbol{P}^{-1}(0)\boldsymbol{P}(T)$, can be equated to a possibly complex matrix $\boldsymbol{B}$:

$$\exp(T\boldsymbol{B}) = \boldsymbol{P}^{-1}(0)\boldsymbol{P}(T) \tag{2.24}$$

Then the fundamental matrix solution can be expressed in the form of:

$$\boldsymbol{P} = \boldsymbol{S}(t)\exp(T\boldsymbol{B}) \tag{2.25}$$

Felix Bloch applied this theorem to the wave function in solid-state physics. The wave function ψ can be expressed as a plane wave modulated by a periodic function:

$$\psi(\boldsymbol{r}) = \exp(ik \cdot \boldsymbol{r})u(\boldsymbol{r}) \tag{2.26}$$

where k is the wave vector, $\boldsymbol{r}$ is a position vector, and i is $\sqrt{(-1)}$. This can be utilized in a perfect crystal where $u(\boldsymbol{r})$ has the same periodicity as the structure of the crystal or in the case of a one-dimensional periodic grating, the period of the grating Λ, as defined in Figure 2.5. This property serves as the basis for solving Maxwell's equations with RCWA in the Transverse Electric (TE) and the Transverse Magnetic (TM) cases.

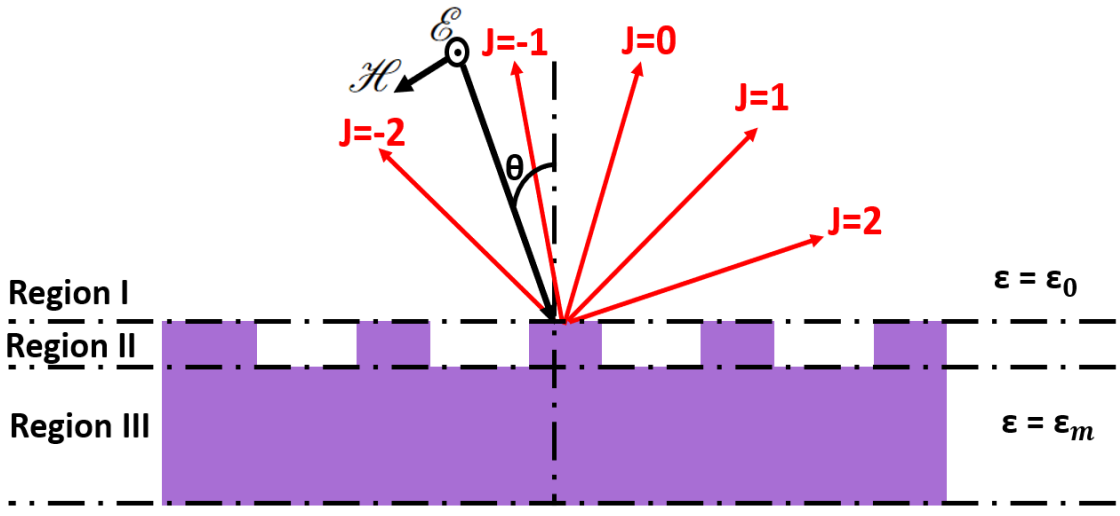

Figure 2.6: TE wave on 1D periodic grating

2.3.1 Transverse Electric

Suppose there is a transverse electric (TE) plane wave incident on a 1D grating at an incident angle θ as seen in Figure 2.6, the dielectric function can be split into three different regions. Region I is free space and has a uniform dielectric function of $\epsilon_r = 1$. Region II has a periodic piece-wise dielectric function of a 1-dimensional position vector x.

$$\epsilon(x) = \begin{cases} \epsilon_r = \epsilon_m \text{ when } x \in 0 \cdot h\Lambda \leq x \leq h\Lambda + f\Lambda \\ \epsilon_r = \epsilon_0 \text{ when } x \notin \cdot h\Lambda \leq x \leq h\Lambda + f\Lambda \end{cases} \tag{2.27}$$

where $[h] = [0, 1, 2, \ldots, \infty]$ and ϵ_m is the dielectric function of the material. $\mathscr{E}$ and H are the normalized incidence electric field and magnetic field with unity magnitude, respectively. This assumption of unitary magnitude means $\mathscr{E}$ can be expressed as $\exp(ik_x x + ik_z z - i\omega t)$ where k_x and k_x are the x and z components of wavevector k. The magnitude of k in regions I and III ca be expressed as:

$$k_I = \frac{2\pi}{\lambda} \tag{2.28}$$

$$k_{III} = \frac{2\pi}{\lambda}\sqrt{\epsilon_m} \tag{2.29}$$

Every k_{xj} satisfies the aforementioned Floquet therom in region I such that:

$$k_{x,j} = \frac{2\pi}{\lambda}\sin\theta + \frac{2\pi}{\Lambda}j \tag{2.30}$$

Factoring out the wave vector, k, from this equation results in the grating diffraction equation:

$$\sin\theta_j = \sin\theta + \frac{j\lambda}{\Lambda} \tag{2.31}$$

where $\theta_j = \sin^{-1}\frac{k_{xj}}{k}$ is the jth order diffraction angle. If $\sin\theta_j > 1$, the result is an evanescent wave, as opposed to a propagating wave, whose field strength decays exponentially with the z direction. Propagating and evanescent diffraction orders must be included in the formulations of RCWA to maintain the continuity of the boundary conditions.

The z components of k are [42]:

$$k_{zj}^r = \begin{cases} \sqrt{k^2 - k_{xj}^2},\ k^2 > k_{xj}^2 \\ i\sqrt{k_{xj}^2 - k^2},\ k_{xj}^2 > k^2 \end{cases} \tag{2.32}$$

where k^r denotes a reflected wave vector. The electric field in region I is a linear combination of the reflected and incident waves:

$$\mathscr{E}_I(x,z) = \exp(ik_x x + ik_z z) + \sum_j \mathscr{E}_j^r \exp(ik_{xj}x - ik_{zj}^r z) \tag{2.33}$$

where $\mathscr{E}^r$ denotes the reflected electric field strength. Then the electric field in region III is the linear combination of transmitted waves.

$$\mathscr{E}_{III}(x,z) = \sum_j \mathscr{E}_j^t \exp(ik_{xj}x + ik_{zj}^t z) \tag{2.34}$$

The electric field in Region II can be expressed as:

$$\mathscr{E}_{II}(x,z) = \sum_j \chi_{yj}(z)\exp(ik_{xj}x)\hat{y} \tag{2.35}$$

Here χ_{yj} is the jth order space-harmonic electric field magnitude in region II. χ_{yj} matches the jth diffraction order previously discussed in regions I and III. The electric field in Equation 2.33, Equation 2.48, and Equation 2.35 can be substituted into Maxwell's equations. RCWA's main objective is to arrange Maxwell's equations

into a summation of phasors of the form $\exp(ik_{xj}x)$, and then set each coefficient to zero for every j. The result of this substitution is an infinite set of second-order coupled equations while each space-harmonic term is coupled with other components through the multiplication of two Fourier series. Ideally, the order of this summation would be ∞. However, this is truncated to make the solution computationally feasible.

The permittivity in Region II will have discontinuities, as it is a piece-wise function based on the periodicity,Λ, of the grating. To overcome these discontinuities the permittivity can be expanded as a Fourier series:

$$\epsilon(x) = \sum_{P} \epsilon_P^{\text{ord}} \exp\left(i\frac{2P\pi}{\Lambda}\right), P = 0, 1, 2, 3, ... \tag{2.36}$$

where ϵ_P^{ord} the Pth Fourier coefficient for the ordinary of $\epsilon(x)$:

$$\epsilon_P^{\text{ord}} = f\epsilon_m + (1-f)\epsilon_0 \text{ when } P = 0$$

or

$$\epsilon_P^{\text{ord}} = \frac{(\epsilon_m - \epsilon_0)\sin(Pf\pi)}{P\pi} \text{ when } P \neq 0$$

ϵ_P^{ord} does not have physical meaning and instead is just a mathematical tool. With this, the coupled-wave equations with Maxwell's equations can be rearranged as the following:

$$\sum_{j}\left(\frac{\partial^2 \chi_{yj}}{\partial z^2} - k_{xj}^2\chi_{yj} + \sum_{P}\epsilon_{j,p}\chi_{y,p}\right)\exp(ik_{xj}, x) = 0 \tag{2.37}$$

A sufficient number of space harmonic orders should be used depending on the desired accuracy and be in agreement with the number of diffraction orders. The agreement in the number of orders allows these equations to be expressed in matrix form:

$$\frac{1}{k^2}\frac{\partial^2 \boldsymbol{X}^y}{\partial z^2} = [\boldsymbol{K}^X\boldsymbol{K}^X - \boldsymbol{E}][\boldsymbol{X}^Y] \tag{2.38}$$

where $\boldsymbol{X}^Y$ is the column vectors formed by χ_{yj}. $\boldsymbol{K}^X$ is a diagonal matrix with elements $\boldsymbol{K}^X_{l,l} = \frac{k_{xj}}{k}$ where $j = l - o_h - 1$. o_h given $N_{\text{orders}} = 2o_h + 1$. $\boldsymbol{E}$ is the matrix generated by the Fourier coefficients of the dielectric function such that $\boldsymbol{E}_{l,m} = \epsilon_P^{ord}$ where the index follows as $P = l - m$. The size of all of these matrices is $N_{\text{orders}} \times N_{\text{orders}}$. $\chi_{y,j}$ can be expressed with the eigenvectors and eigenvalues of the above matrices.

$$\chi_{y,j}(z) = \sum_{l=1}^{N} V^A_{j,l}[C_l^{A+} \exp(k\xi_l(z-d))k + C_l^{A-} \exp(-k\xi_l z)] \tag{2.39}$$

$V^A_{j,l}$ are the elements of the matrix $\boldsymbol{V}^A$ which is composed of the eigenvector corresponding to the eigenvalue for the matrix $[\boldsymbol{K}^X\boldsymbol{K}^X - \boldsymbol{E}]$. The C's are the unknown coefficients of exponential terms that represent the forward and backward coupled diffracted waves in Region II, using +, - to denote them respectively. $\boldsymbol{Q}$ is the matrix of positive square roots of the eigenvalues of $[\boldsymbol{K}^X\boldsymbol{K}^X - \boldsymbol{E}]$. ξ_l represents the diagonal values of $\boldsymbol{Q}$.

Region II can have its magnetic field written in the form of:

$$\mathscr{H}_{II}(x,z) = i\frac{k}{\mu_0\omega}\sum_j [\gamma_{x,j}(z)\hat{\boldsymbol{x}} + \gamma_{z,j}(z)\hat{\boldsymbol{z}} \exp(ik_{xj}x)] \tag{2.40}$$

where γ_{xj} and γ_{zj} are the x and z component of the jth order space-harmonic of the electric field in Region II. Expanded this is the following:

$$\gamma_{xj}(z) = \sum_{l=1}^{N} W^A_{j,l}[C_l^{A+} \exp(k\xi_l(z-d))k + C_l^{A-} \exp(-k\xi_l z)] \tag{2.41}$$

where $W^A_{j,l} = \boldsymbol{Q}V^A_{jl}$. The diffraction efficiencies of the grating can be found by solving for $C_l^{A+}, C_l^{A-}, \mathscr{E}_{rj}, \mathscr{E}_{tj}$ for each diffraction order, for a total of $4{\cdot}N$ unknowns. Using the continuity boundary conditions between each region, the diffraction efficiency for the jth order reflected wave and transmitted wave can be obtained by its time-averaged

Poynting vector[42]:

$$\mathrm{DE}_j^r = \mathscr{E}_j^r \mathscr{E}_j^{r*} \mathrm{Re} \frac{k_{zj}^r}{k \cos\theta} \tag{2.42}$$

$$\mathrm{DE}_j^t = \mathscr{E}_j^t \mathscr{E}_j^{t*} \mathrm{Re} \frac{k_{zj}^r}{k \cos\theta} \tag{2.43}$$

It should be noted that since the beam output plane is different from the plane of incidence, in general, the polarization status of the diffracted waves will be different from the incident wave. The directional-hemispherical reflectance and transmittance can be obtained by:

$$R = \sum \mathrm{DE}_j^r \tag{2.44}$$

$$T_m = \sum \mathrm{DE}_j^t \tag{2.45}$$

For all of the gratings considered in this study, the substrate is assumed to be opaque, so the emittance is:

$$\epsilon(\theta, \phi, \lambda) = 1 - R(\theta, \phi, \lambda) \tag{2.46}$$

2.3.2 Transverse Magnetic

Figure 2.7 shows a transverse magnetic (TM) wave incident on a 1D grating. Here the oscillation direction of the magnetic and electric fields is switched from the TE case. Typically the TM polarization case of gratings tends to exhibit more dramatic optical properties than the TE case.

The magnetic field in region I is:

$$\mathscr{H}_I(x, z) = \exp(ik_x x + ik_z z) + \sum_j \mathscr{H}_j^r \exp(ik_{xj} x - ik_{zj}^r z) \tag{2.47}$$

where $\mathscr{H}^r$ denotes the reflected magnetic field strength. Then the magnetic field in

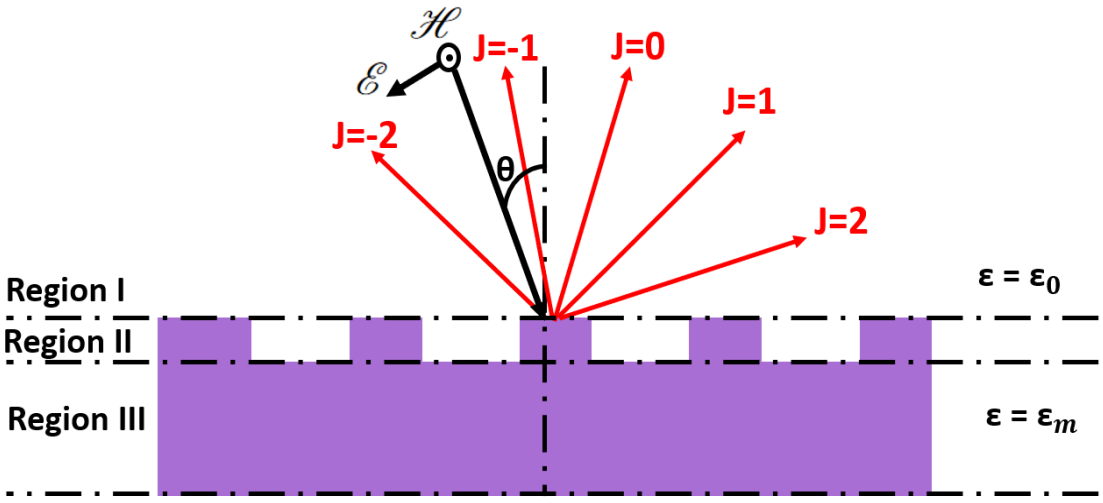

Figure 2.7: TM wave on 1D periodic grating

region III is the linear combination of transmitted waves.

$$\mathscr{H}_{III}(x,z) = \sum_j \mathscr{H}_j^t \exp(ik_{xj}x + ik_{zj}^t z) \tag{2.48}$$

where $\mathscr{H}_j^t$ is the jth order transmitted field strength. The magnetic field in Region II can be expressed as:

$$\mathscr{H}_{II}(x,z) = \sum_j \gamma_{yj}(z)\exp(ik_{xj}x)\hat{y} \tag{2.49}$$

Due to the rules of Fourier Coefficients, the dielectric functions' discontinuities are expressed with the inverse of the dielectric function:

$$\epsilon^{\text{inv}}(x) = \frac{1}{\epsilon(x)} = \sum_p \epsilon_P^{\text{inv}} \exp\left(i\frac{2P\pi}{\Lambda}x\right) \tag{2.50}$$

where ϵ_P^{inv} pth Fourier coefficient for the inverse of $\epsilon(x)$. Similar to the previous TE,

solving Maxwell's equations using the previous equation results in:

$$\sum_j (\sum_P \epsilon_{j,P}^{inv} \frac{\partial^2 \gamma_{yP}}{\partial z^2} - \sum_P k_{xj} (\epsilon^{ord})_{jP}^{-1} k_{xP} \gamma_{yP} + k^2 \gamma_{yj}) \exp(ik_{xj}x) = 0 \tag{2.51}$$

These equations can be solved in a similar matrix form. Again, the diffraction efficiencies are the time-averaged Poynting vectors[42]:

$$\mathrm{DE}_j^r = \mathscr{E}_j^r \mathscr{E}_j^{r*} \mathrm{Re} \frac{k_{zj}^r}{k \cos\theta} \tag{2.52}$$

$$\mathrm{DE}_j^t = \mathscr{E}_j^t \mathscr{E}_j^{t*} \mathrm{Re} \frac{\epsilon_0 k_{zj}^r}{\epsilon_m k \cos\theta} \tag{2.53}$$

Again, the directional-hemispherical reflectance and transmittance can be obtained by:

$$R = \sum \mathrm{DE}_j^r \tag{2.54}$$

$$T_m = \sum \mathrm{DE}_j^t \tag{2.55}$$

2.3.3 Conical Diffraction

A unique scenario occurs when the polarization of the incident wave does not line up with the orientation of the grating (ie. the azimuthal angle, $\phi \neq 0, \pi/2$). A plane of incidence can be established, defined by the vector $[\cos\phi, sin\phi, 0]$ for these cases. The majority of the diffracted waves ($j \neq 0$) do not lie in the plane of incidence, instead, they form a cone centered around the grating grooves. It is convenient to establish polarization in these cases with an angle Ψ, which is the angle between the electric field vector and the plane of incidence. This angle translates to the previously discussed TE wave when $\Psi = 90^o$ or a TM wave when $\Psi = 0^o$. All other linear polarizations can be decomposed into these two polarizations.

Solving Maxwell's equations in the conical case is extremely similar to the TE and TM cases, except the electric field has x,y, and z components. The electric field in region I is:

$$\mathscr{E}_I(x,y,z) = \exp(ik_x x + ik_y y + ik_z z) + \sum_j \mathscr{E}_j^r \exp(ik_{xj} x + ik_y y - ik_{zj}^r z) \tag{2.56}$$

Subsequently the electric field in region III is:

$$\mathscr{E}_{III}(x,y,z) = \sum_j \mathscr{E}_j^t \exp(ik_{xj} x + ik_y y + ik_{zj}^t z) \tag{2.57}$$

Again, the electric field in region II can be expressed as a Fourier series:

$$\mathscr{E}_{II}(x,y,z) = \sum_j [\chi_{xj}(z)\hat{x} + \chi_{yj}(z)\hat{y} + \chi_{zj}(z)\hat{z}] \exp(ik_{xj} x + (ik_{yj} y)) \tag{2.58}$$

as can the magnetic field:

$$\mathscr{H}_{II}(x,y,z) = i\sqrt{\frac{\epsilon_0}{\mu_0}} \sum_j [\gamma_{xj}(z)\hat{x} + \gamma_{yj}(z)\hat{y} + \gamma_{zj}(z)\hat{z}] \exp(ik_{xj} x + (ik_{yj} y)) \tag{2.59}$$

In the previous section, obtaining the diffraction efficiencies required $4 \cdot N$ unknowns to be solved for. In the conical case, $10 \cdot N$ coefficients need to be solved for. This significantly increases the computational time required to obtain the diffraction efficiencies. This leads to the hemispherical optical properties of gratings being quite computationally expensive to determine with RCWA.

2.4 Basic Fundamentals of Neural Networks

The atomic unit of neural networks is the neuron, named after their original biological inspiration. Essentially these neurons take in input data, perform calculations on that data and then output the result. Neural networks are a series of neurons connected in various patterns to emulate a desired data manipulation operation, this can be as simple as emulating an analytical function or a more complex application of recognizing handwriting. Typically these neurons are organized in layers, an input layer to receive the data, hidden layers to manipulate the data, and an output layer to pass the result.

The neurons in each layer base their value on the previous neurons. How much each neuron influences the current neuron is represented in a collection of weights w. Then all of the inputs to the neuron are summed together and combined with a bias b. Then an activation function is applied to determine the value of the neuron. The weights and biases are determined using training data. For example, given a set of input and output data, each training iteration will try to manipulate the weights and biases to minimize the difference between the ground truth and the output neuron values. The numerical evaluation of the difference is done with what is referred to as a loss function. The loss function is determined based on what type of error should be punished more. For example, mean squared error punishes large mistakes more than small ones. The neural net is trained from the output layer backwards to the input layer through a process called backpropagation. Each layer has the derivative of the cost expressed as a product of derivatives between each layer. A manipulation of the weights provides a simple modification of these partial products. Thus the weights are manipulated to reduce the backwards propagating error (backpropagation). The activation functions make training easier by introducing non-linearity into the possible values of a neuron. These activation functions must be monotonic, differentiable,

and quickly converging for backpropagation to work.

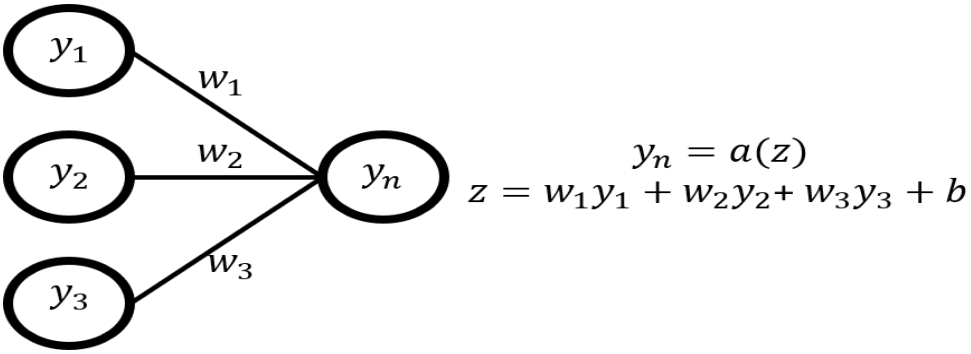

Figure 2.8: Single layer Perceptron

CHAPTER 3
INVERSE DESIGN AND OPTIMIZATION METHODS

Gratings are incredibly simple and complex at the same time. Every TPV system has different requirements and optimal optical characteristics for its employed emitter. This is an inverse problem, the optical properties are the starting point and the parameters are to be calculated. These optimal properties might not even be possible/feasible, instead, the best grating to emulate these properties is desired. Therefore, the introduction of a function $F(\boldsymbol{s})$ where $\boldsymbol{s} = [\Lambda, f, d]$ that can quantitatively assess the utility of a grating is required, is often referred to as an objective function, loss function, or fitness function. In the case of gratings, the optical properties can be determined with the aforementioned (RCWA) calculations. Determining the forward mapping $\boldsymbol{s} \rightarrow F$ of this problem is relatively easy, however the inverse $F \rightarrow \boldsymbol{s}$ is often extremely difficult if not impossible, this is coupled with the fact the most real-world loss functions are relativistic and intended to compare solutions against one another. The inverse design problem is solved by optimizing F, this chapter discusses the techniques and challenges associated with this optimization.

3.1 Emitter Optimization Techniques

There are two main classes of optimization, continuous and discrete. Continuous optimization problems have an uncountable number of possible parameters, $\boldsymbol{s}$. Discrete problems have a finite number of possible parameters, $\boldsymbol{s}$, for instance, the number of ways to order a multi-layer emitter composed of a finite number of layers [43]. Gratings on the other hand can theoretically have an infinite number of possible parameters. In the real world, the parameters are bounded by the manufacturing

resolution, meaning the units of the parameters are actually countable. Problems like these are referred to as quasi-continuous. For the purposes of this study, the manufacturing tolerances of Tungsten gratings are assumed to be 10nm. For example, a grating could have a period, Λ, of $1.47\mu m$, but another grating with $\Lambda = 1.473\mu m$ would be rounded and considered an equivalent to $\Lambda = 1.47\mu m$.

A local minimum can be defined as $F(\boldsymbol{s}_*) \geq F(\boldsymbol{s})$ for all $\boldsymbol{s}$ with in any non zero difference, $\Delta > 0$, of $\boldsymbol{s}_*$. A local maximum can be defined as $F(\boldsymbol{s}_*) \leq F(\boldsymbol{s})$ for all $\boldsymbol{s}$ with in any non zero difference, $\Delta > 0$, of $\boldsymbol{s}_*$. In terms of optimization, these problems are equivalent. Maximization problems can be transformed into minimization problems by simply reflecting the loss function about the x-axis. The same can be done to transform minimization problems into maximization problems. The optimization problems presented in this study will be framed as minimization problems.

Oftentimes, local minimization utilizes convex optimization techniques to find minima. Typically these are based on the assumption that the function is differentiable. First-order algorithms involve the gradient of the function, usually estimated by sampling, to determine which direction to move in the next algorithm iteration. These algorithms often converge on local minima or oscillate indefinitely depending on the shape of the objective function and the starting conditions. Famous algorithm examples of these include stochastic gradient descent, and adam [44]. There are also second-order algorithms based on the hessian, to determine the movement direction; examples include Newton's method and secant method.

The above algorithms excel at finding local minima, for a relatively cheap computational cost. However, when optimizing emitters the loss function is almost always multimodal, and a local minimum may be much greater than the global minimum. A global minimum can be defined as a point $\boldsymbol{s}_*$ such that $F(\boldsymbol{s}_*) < F(\boldsymbol{s})$ for all possible $\boldsymbol{s}$. Therefore, an algorithm that can identify global optima is desired. Some tech-

niques for this include deterministic pattern search algorithms. One of the simplest methods is a parameter sweep, this has been used to design the geometry of a grating[6] and the operating conditions of the TPV system [45]. These methods try to map out the entire operating space of feasible solutions through essentially a guided pattern search. These algorithms typically search a problem space in a systematic fashion. Even with the simple nature of gratings, there can be millions of possibilities in relatively small design spaces, making complete pattern search algorithms infeasible and partial searches resulting in information holes. This prompts the use of heuristic methods to find approximate solutions when classical methods fail to find any exact solution. Heuristic methods are often stochastic in nature, meaning how well the algorithm performs on a given problem can change based on how "lucky" the algorithm got. Most heuristic methods also do not rely on the objective function to be differentiable, allowing them to be applied to a wide range of applications and problems.

3.1.1 Metaheuristics

Several common Metaheuristic methods and algorithms have been applied to TPV optimization. Nguyen et. al. applied a genetic algorithm (GA) to optimize 1D Tungsten gratings [7]. Genetic Algorithms have also been used to optimize the thickness and doping characteristics of the photovoltaic cell [46]. Particle swarm optimization (PSO) is another widely implemented algorithm for emitter design optimization [47]. All of these algorithms are examples of metaheuristics, a higher-level procedure that combines simple heuristics to create a search algorithm. Other well-known examples of metaheuristics include: differential evolution, simulated annealing, ant colony optimization, firefly optimization, and scatter search. Fundamentally all these algorithms can be expressed as a collection of low-level heuristics.

Consider all possible candidate solutions to a problem,$\mathfrak{S}$. Although, a little abstracted, this can be mathematically defined as:

$$\mathfrak{S} = \{\boldsymbol{s} \in \mathbb{R}^D : (\exists L, U \in \mathbb{R}^D [L \leq \boldsymbol{s} \leq U])\} \tag{3.1}$$

where L and U are the lower and upper bounds of the problem in real space and D is the dimensionality of the solutions. Simple Heuristics (SH) are the simplest unit of search algorithms. There are two classes of simple heuristics: constructive and perturbative. Constructive SH aim to generate new candidate solutions while perturbative change existing solutions into ideally a better one[48]. A constructive SH can be represented as

$$h(\mathfrak{S}) \rightarrow \boldsymbol{s}(t) \tag{3.2}$$

where t is the algorithm iteration. A perturbative SH can be represented as:

$$\boldsymbol{s}(t) \rightarrow h(\boldsymbol{s}(t), \mathfrak{S}) \rightarrow \boldsymbol{s}(t+1) \tag{3.3}$$

These simple heuristics can be combined together to form a Metaheuristics (MH). A Metaheuristics can be defined as an iterative procedure, composed of a finite sequence of simple heuristics, that renders an optimal solution $\boldsymbol{s}_*$ for a given optimisation problem[48]. Figure 3.1 shows the structure of how simple heuristics can be combined into a Metaheuristic (MH). h_o is referred to as the initializer, often times this is a constructive heuristic that generates candidate solutions randomly or according to some pattern. Common patterns used are the vertexes of the solution space $\mathfrak{S}$ or diamond patterns around the centroid of $\mathfrak{S}$. h_f, referred to as the finalizer, evaluates the quality of a solution base on the current value of $F(\boldsymbol{s(t)})$ and information about the previous values of F i.e. ($F(\boldsymbol{s(t-i)})$) where $i \in \mathbb{N}$. The finalizer determines if subsequent iterations are needed. If this is determined the current position,

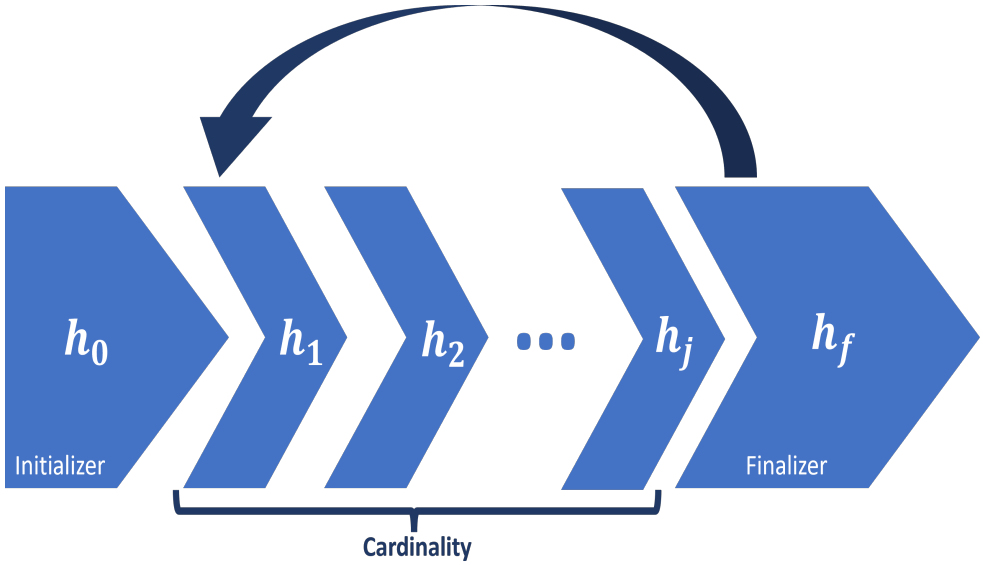

Figure 3.1: Architecture of a Metaheuristic

$\boldsymbol{s}(t)$, is used in place of the initializer in subsequent iterations. An example algorithm of how all these pieces fit together is given in Algorithm 1.

Algorithm 1 Sample Optimization Algorithm composed of Simple Heuristics

$n \leftarrow$ population index
$N_{\text{pop}} \leftarrow$ population size
$t \leftarrow$ current iteration
$\boldsymbol{p} \in \mathfrak{P}$ A parameter in a collection of parameters governing the simple heuristics
$\forall$ n $\boldsymbol{s}_n = U(\mathfrak{S})$ Generates random candidate solutions uniformly across $\mathfrak{S}$

while $t \leq t_f$ **do**
  $\boldsymbol{s}_n(t+1) \leftarrow h_1(\boldsymbol{s}_n(t), \boldsymbol{p})$
  ...
  $\boldsymbol{s}_n(t+1) \leftarrow h_j(\boldsymbol{s}_n(t), \boldsymbol{p})$
  if $F(\boldsymbol{s}_n(t)) < \boldsymbol{s}_n(t+1)$ **then**
    $\boldsymbol{s}_n(t+1) = \boldsymbol{s}_n(t)$
  end if

3.2 Creating Metaheuristic Optimization Algorithms with Hyper-heuristics

Typically when new optimization algorithms are created, the status quo has been for the architect to take inspiration from naturally occurring phenomena, as an anal-

ogy for a data manipulation process. Basically, any animal has an associated optimization algorithm, a suggested exercise to prove this would be to think of any animal, add optimization after it, and search for publications. However, oftentimes, the utility of these optimization algorithms leads much to be desired. According to the "no-free lunch" theorem, any given metaheuristic optimization algorithm has equivalent performance compared to any other algorithm averaged over all possible problems. In other words, an algorithm's utility is dependent on the problem, and the problem should be considered when creating a new optimization algorithm.

Using the building block model of a metaheuristic optimization algorithm, as seen in Figure 3.1, new algorithms can be algorithmically constructed. This is extremely similar to the optimization problem previously discussed. The possible solutions are the different ways to order simple heuristics to make an algorithm of a given cardinality. Then a cost function is used to evaluate the performance of the algorithm, typically a statistic capturing the average function value of the original problem given a number of iterations. A discrete heuristic optimization algorithm can be used to search over the algorithm possibilities. This procedure of using heuristics to select heuristics is commonly referred to as a Hyper-heuristic.

3.2.1 Ideal Emittance Spectrum Problem

Consider a TPV system composed of a Tungsten grating, and a $In_{0.18}Ga_{0.82}Sb$ cell with a band gap of 0.56eV. The grating period that is going to be appropriate in exciting SPP with positive and negative diffraction orders is [7]:

$$\Lambda > \frac{j\lambda}{n_{\text{index}}}, j > 0 \tag{3.4}$$

$$\frac{|j|\lambda}{2n_{\text{index}}} < \Lambda < \frac{|j|\lambda}{n_{\text{index}}}, j < 0 \tag{3.5}$$

The cavity resonance effects from the interference of the diffracted waves have a corresponding wavelength given by [49]:

$$\lambda_{m,n} = \frac{2}{\sqrt{(l/w)^2 + (m/d)^2}} \tag{3.6}$$

where w is the grating with such that $w = \Lambda \cdot f$, and d is the depth. l and m determine the contributions of the width and depth to this frequency. Wood's anomaly causes abrupt changes in the optical properties of the grating and can be predicted with [50]:

$$(\frac{\lambda j}{\Lambda})^2 = 2\frac{\lambda}{\Lambda} j \sin\theta - \cos^2\theta \tag{3.7}$$

It is ideal that the dominant frequency of grating is just above the bandgap of the PV cell. If it too close to the bandgap significant energy can be lost, therefore the previous equations can be used to generate a design space of the possible grating parameters.

$$\mathfrak{S}(\Lambda, f, d) = \begin{cases} \Lambda \;\; 0.3\mu m \leq \Lambda \leq 2.0\mu m \\ f \;\; 0.1 \leq f \leq 0.9 \\ d \;\; 0.3\mu m \leq d \leq 2.0\mu m \end{cases} \tag{3.8}$$

An idealized normal emittance was used to evaluate the gratings, that is an emittance of 1 above the bandgap and an emittance of zero below the bandgap.

$$TE_{id} = \begin{cases} 1 \;\; 600nm \leq \lambda \leq 2200nm \\ 0 \;\; 2200nm \leq \lambda \leq 4000nm \end{cases} \tag{3.9}$$

$$TM_{id} = \begin{cases} 1 \;\; 600nm \leq \lambda \leq 2200nm \\ 0 \;\; 2200nm \leq \lambda \leq 4000nm \end{cases} \tag{3.10}$$

The optical properties are determined with RCWA, using 100 evenly spaced data points from $0.6\mu m$ to $2.2\mu m$. This translates to 47 data points below the bandgap and 53 data points above the bandgap. Again, 40 positive and negative diffraction orders were also used. The difference between the actual emittance and idealized can be quantified with a discretized least squares summation:

$$\begin{aligned}
\min_{\Lambda,f,d} F(\boldsymbol{s}) = w_1 \sum_{1}^{j} \frac{1}{j}(\mathrm{TE}_{act} - \mathrm{TE}_{id})^2 + w_2 \sum_{1}^{k} \frac{1}{k}(\mathrm{TE}_{act} - \mathrm{TE}_{id})^2 \\
+ w_1 \sum_{1}^{j} \frac{1}{j}(\mathrm{TM}_{act} - \mathrm{TM}_{id})^2 + w_2 \sum_{1}^{k} \frac{1}{k}(\mathrm{TM}_{act} - \mathrm{TM}_{id})^2 \\
\text{Subject To: } 0.3\mu m \leq \Lambda \leq 2.0\mu m \\
0.1 \leq f \leq 0.9 \\
0.3\mu m \leq d \leq 2.0\mu m \\
w_1 = 0.5 \\
w_2 = 0.5 \\
j = 47 \\
k = 53
\end{aligned} \tag{3.11}$$

where TE_{act} and TM_{act} is the emittance for a particular wavelength as determined by RCWA for transverse electric and transverse magnetic polarizations.

3.2.2 Hyper-heuristic Methodology

A Hyper-heuristic (HH) algorithm was applied to the problem outlined insubsection 3.2.1, with the goal of creating a more efficient optimization algorithm for similar problems than common existing methods seen in the literature. The cost function of an algo-

rithm was designed to be:

$$75\%\text{tile of } \bigcup_{1}^{100} F(\boldsymbol{s}^*)|t = 10 \tag{3.12}$$

This equation represents the function value the algorithm should achieve or beat 75% of the time given 10 iterations based on 100 sample runs. Then a discrete simulated annealing algorithm was applied to globally search over the possible algorithms. Possible algorithms being those composed of less than 2 simple heuristics and having a population size of 8.

A python software package called CUSTOMHys [48] was used to for the Hyper-heuristic implementation and provided a data set of simple heuristics extracted from common optimization algorithms. Figure 3.2 shows the structure of our initial Hyper-heuristic applied to the problem outlined in subsection 3.2.1. One thing to notice about the procedure is the extensive use RCWA, to evaluate 1 Algorithm with the Hyper-heuristic framework would require 1.6 million individual RCWA calculations of the spectral emittance. This is essentially impossible with the computational resources available to most. Therefore, a computationally quicker replacement for RCWA is required to facilitate the Hyper-heuristic.

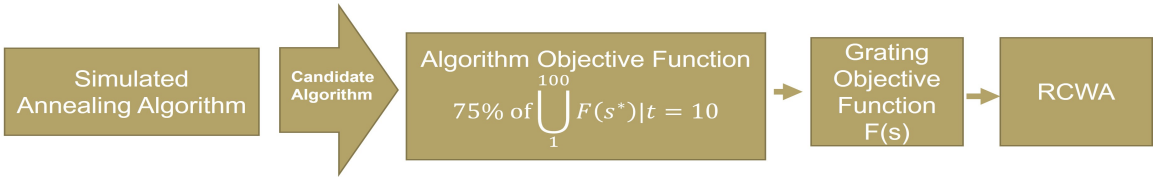

Figure 3.2: Initial Hyper-heuristic Structure

3.2.3 RCWA Surrogate

It can be famously shown that neural networks can emulate any function to an arbitrary accuracy given enough training data, allowing them to be used as a

"surrogate" for physics-based simulations and calculations. Recurrent neural networks(RNN) models have the outputs of neurons and cycle back to feed into the inputs. RNNs are commonly used for physics simulations [51], as these models try to show how a system evolves over time. An extremely popular type of RNN, Long Short-Term Memory (LSTM) networks have been extensively applied to sequence prediction and modeling [52]. However, in the case of an RCWA surrogate, the various data points have no temporal relationship so these more complex model architectures are not needed. Another widely popular neural net feature is convolutions (CNN), similar to RNNs, but RNNs have infinite impulse response while CNNs have a finite response. CNNs are typically used with data that has a spatial relationship. Again, this is not applicable to creating a RCWA surrogate and instead, a fully connected neural net (FCNN) model was used, as seen in Figure 3.3.

This FCNN has 9 input neurons representing the geometry of a grating, angle of incidence, azimuthal angle of incidence, polarization, wavelength, and the complex and real parts of the dielectric function of Tungsten at that wavelength. In this model, every single neuron affects every neuron in the next layer. The 9 input neurons are connected to 3 hidden layers of size 512, 1024, and 1024 in order of their propagation. The sizes of these layers were determined with a highly advanced optimization algorithm called "Graduate Student Search", in which a graduate student tried out different model parameters to identify what worked the best.

Each neuron in the hidden layers used a Leaky Rectified Linear Unit (LReLU) activation function. LReLU, as seen in Figure 3.4c, provides quick training convergence and non-linearity, albeit slightly slower than Rectified Linear Unit (ReLU), Figure 3.4b. However, LReLU does not have the problem of "dead ReLU". This is where the input values into the activation function are always < 0, and the partial derivatives for the backpropagation algorithm are always zero. Dead Relu is mostly a

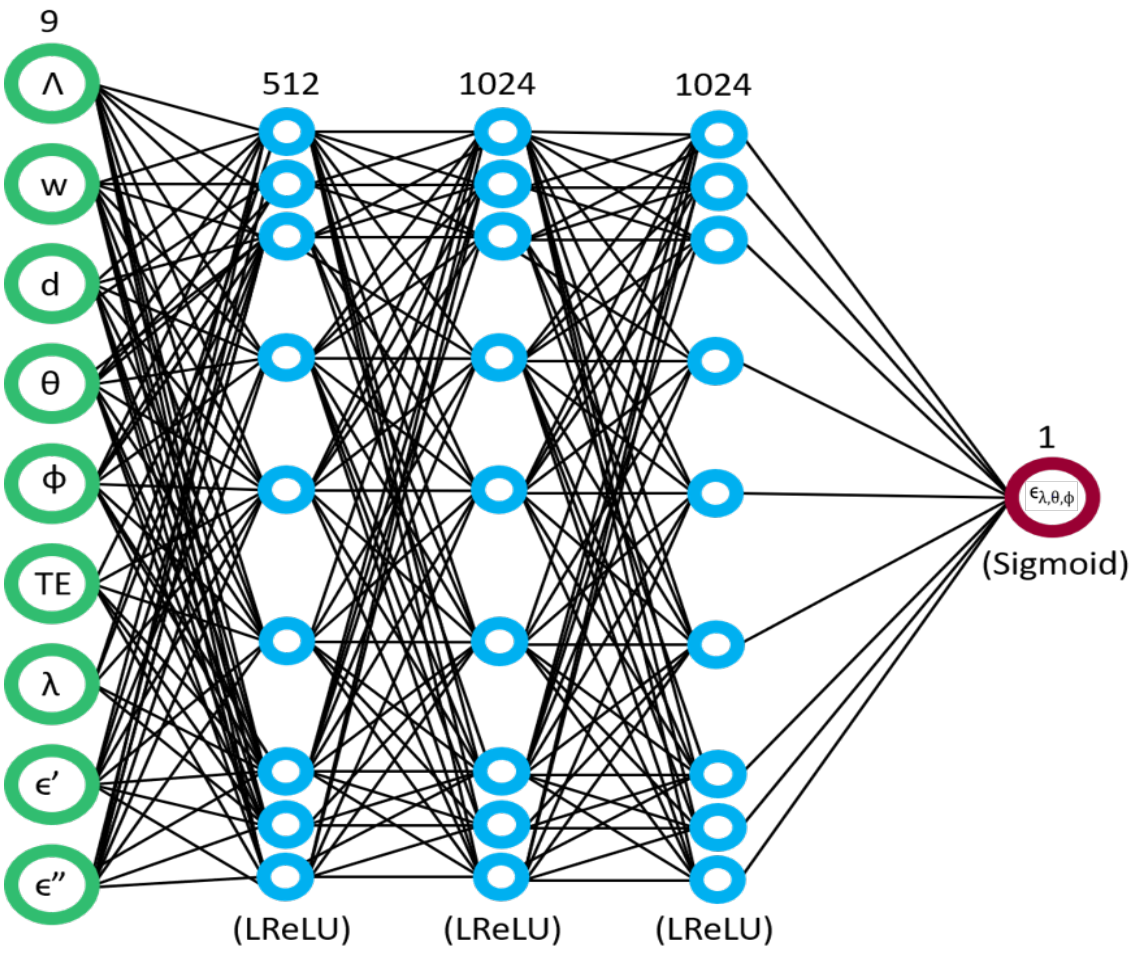

Figure 3.3: RCWA Surrogate Model Architecture

concern with image pixel data, and can actually be advantageous in certain scenarios as it introduces "optimal brain damage" to regularize and simplify the model.

The output neuron used a Sigmoid activation function, as seen in Figure 3.4a. Sigmoid is a traditional "old school" activation function that has been phased out in favor of functions with faster convergence. Sigmoid squishes the input data into values between 0 and 1, making it uniquely applicable for representing the emittance property. Since Sigmoid is just used for a single neuron is going to have a negligible effect on training speed. Sigmoid also does not require consideration for dead neurons like ReLU as some slope is present for all function values. This ensures that the

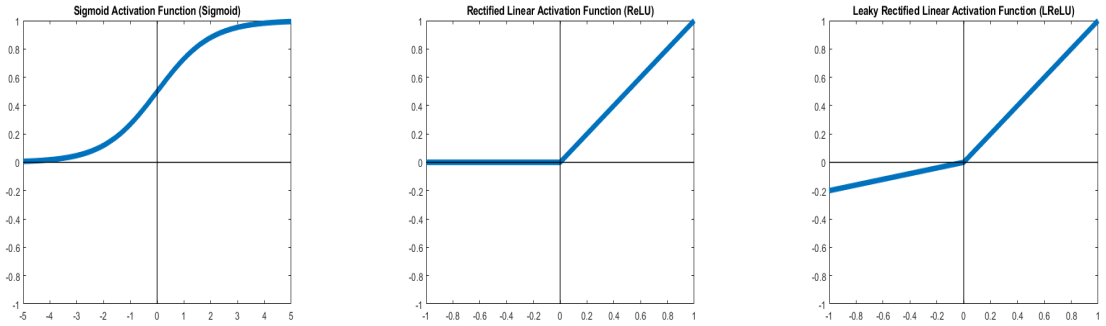

(a) Sigmoid (b) ReLU (c) LReLU

Figure 3.4: Activation Functions

neuron can still learn from near-zero activation function value cases.

The data set for the FCNN model was built in a pseudo-active manner. Tungsten gratings were optimized according to the problem in subsection 3.2.1, and the RCWA calculations were then saved in the database. The database served 2 purposes, future calculations can query the database to prevent duplication, and training data, which is biased toward the desired application of the FCNN model, is generated. Training was done using MSELoss:

$$\text{MSE Loss}(x, y) = (x - y)^2 \tag{3.13}$$

where x is the ground truth and y is the model's guess. This punishes the model for making big mistakes. L1Loss was used as a visualization tool for testing purposes, as it can be quit hard to decipher the meaning of MSEloss numbers. L1loss is simply:

$$\text{L1Loss}(x, y) = |x - y| \tag{3.14}$$

where x is the ground truth and y is the model's guess. Testing was done on a data set of approximately 20% of the size of the training data set. The training set was also supplanted with emittance values of completely unique gratings. This

was done to ensure that the model was actually learning RCWA calculations and not simply interpolating between data points, and to evaluate its effectiveness at handling gratings it has zero training data on.

Table 3.1: FCNN Model Accuracy

# of Training Points [10^6]	Test Avg MSE Loss	Test Avg L1 Loss	Epochs	Batch Size
0.16	0.001517	0.038951	50	1024
0.32	0.000878	0.029631	50	1024
0.48	0.000504	0.022449	50	1024
0.64	0.000344	0.018547	50	1024
0.80	0.000252	0.015874	50	1024
0.96	0.000193	0.013892	50	1024
1.12	0.000152	0.012328	50	2048
1.28	0.000128	0.011313	50	2048
1.6	0.0000498	0.007056	500	2048

The accuracy results for different training conditions are outlined in Table 3.1, to show the relationship between the amount of training data and the accuracy of the FCNN model. The models were trained with the Adam optimizer algorithm for the backpropagation over a variety of epochs and batch sizes. The models were trained on a RTX 3070 graphical processing unit (GPU), with 5888 CUDA cores, this allowed most of the models to be trained in a couple of hours, obviously depending on the amount of training data and number of epochs. Unsurprisingly, the model's accuracy increases with more data. However, it is quite interesting how accurate the model is with a relatively low amount of data. An average L1loss of < 0.02 was able to be achieved with just 640,000 data points. The model trained with 1.6 million data points over 500 epochs achieved an average test MSEloss of 0.007. An example of this FCNN model's output compared with the native RCWA calculations is depicted in Figure 3.5. The model struggles with detecting the smaller features of an emit-

tance spectrum. Despite this the data definitively shows that FCNN can be used as RCWA surrogates. The final model, (last row in Table 3.1) was determined to be of acceptable quality for use in the Hyper-heuristic creation of new optimization algorithms. Passing data through the model was done on the same graphical processing unit (GPU) used for training. 100 native RCWA calculations took about 2 seconds on an i7 6700 CPU with 4 cores, while 100 surrogate RCWA calculations takes about 0.002 seconds with the FCNN model.

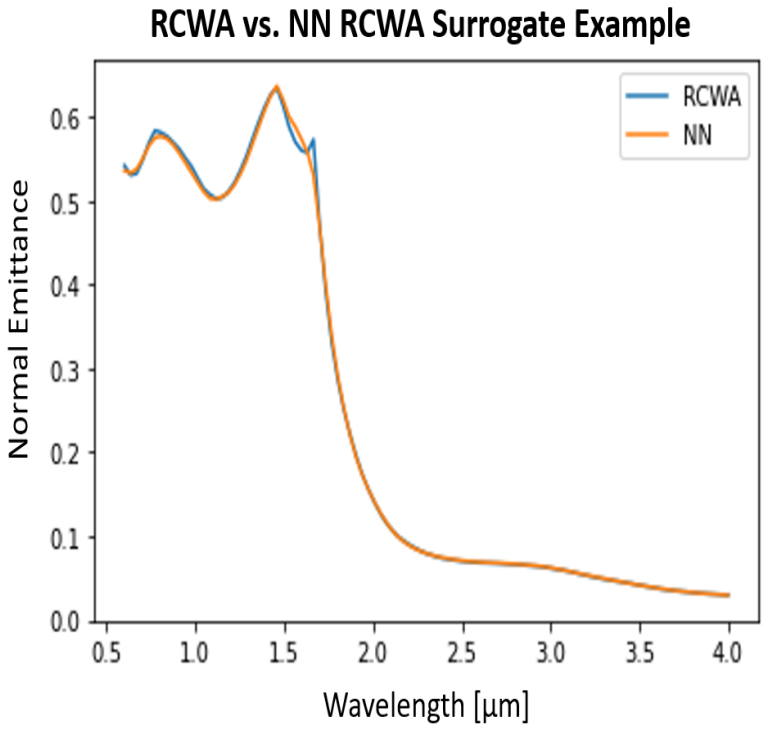

Figure 3.5: RCWA Surrogate Performance

3.3 Hyper-heuristic Results

The Hyper-heuristic framework described in subsection 3.2.2 and depicted in Figure 3.2 was performed with the FCNN model, as seen in the last row of Table 3.1, in place of the native RCWA calculations. After about 500 iterations of the simulated annealing Hyper-heuristic algorithm a new algorithm was generated composed of the

following simple heuristics[53]:

$$h_1 : \mathbf{s_n}(t+1) = \mathbf{s}_*(t) - \vec{r}\boldsymbol{R}_D(\theta)(\boldsymbol{s}(t) - \boldsymbol{s}_*(t)) \tag{3.15}$$

where $R_D(\theta)$ is the rotation matrix determined by the product of all the combinations of two-dimensional rotation matrices by utilizing Euler-Rodrigues's rotation formula, $\mathbf{s}_*(t)$ is the best solution of the population, $\vec{r}$ is a uniformly distributed random vector $\vec{r} = r_i \sim U(r_0 - \sigma, r_0 + \sigma)$ and $r_o = 0.9, \sigma = 0.1, \theta = 22.5^o$. This is referred to as a spiral dynamic heuristic. This was linearly followed by a differential mutation simple heuristic:

$$h_2 : \mathbf{s_n}(t+1) = \mathbf{s}_{z_1}(t) + F \cdot (\mathbf{s}_*(t) - \mathbf{s}_{z_2}(t)) + F \cdot \sum_{m=1}^{M} (\mathbf{s}_{z_{2m+1}}(t) - \mathbf{s}_{z_{2m+2}}(t)) \tag{3.16}$$

where $F = 1$ is the "strength" of the mutation, $M = 1$ is the number of Mutations, and $z_i \sim U(1, N)$ is a random member of the population of solutions. This heuristic essentially randomly mutates a random agent toward the best solution.

These heuristics were paired with a uniform random initializer to generate the first population of solutions. Due to the nature of the cost function evaluating the utility of the algorithms, the combination of these heuristics balance exploitation and exploration. The Spiral dynamic heuristic mostly serves to explore new solutions, while differential mutation is more exploitative. The combination of both however is where the strength of this algorithm comes from. The objective function values from 100 optimization runs using this algorithm, with a population size of 8, were collected to serve as an indication of this algorithm's performance. Figure 3.6 shows the interquartile range of this data.

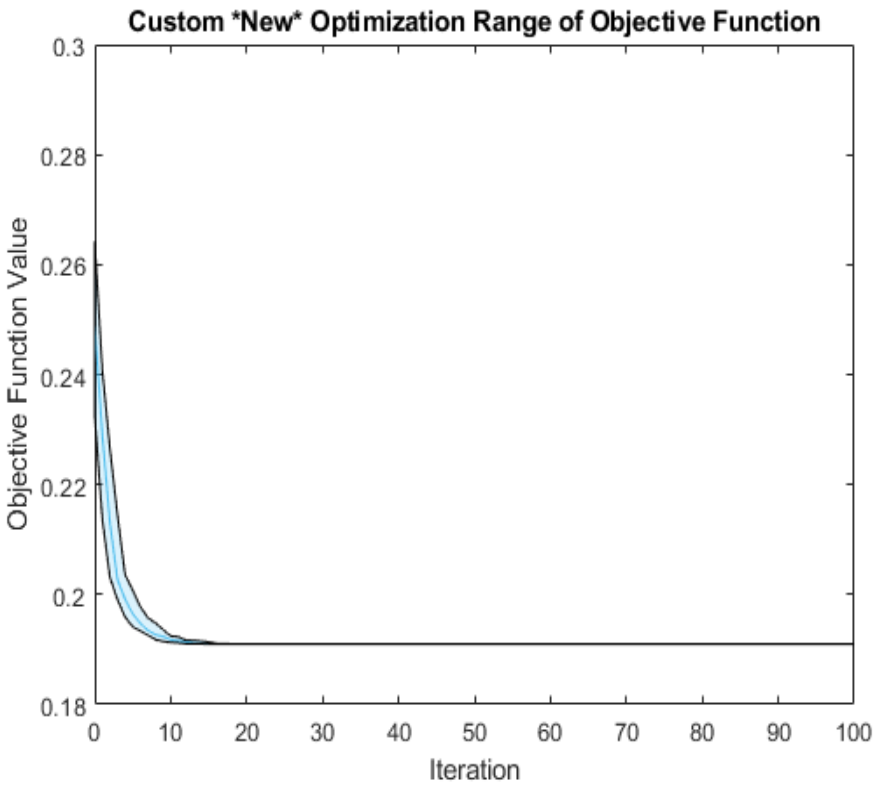

Figure 3.6: Custom Algorithm Interquartile Range

3.4 Metaheuristic performance comparison

The algorithm created in section 3.3 was compared to several well know metaheuristics algorithms with non-optimized parameters: simple uniform random search (RS), single point crossover genetic algorithm (GA), inertial particle swarm optimization (PSO), firefly optimization (FA), and differential evolution (DE). These were selected based on what is commonly used in the literature for optimizing gratings, with the addition of random search. All of these methods were implemented with a population size of $N = 8$.

3.4.1 Uniform Random Search

Random search serves as the ultimate baseline for an evaluation of heuristics, it represents the values you would get just uniformly randomly guessing solutions. The heuristic that represents this mathematically is:

$$h_1 : \mathbf{s_n}(t+1) = U(\mathfrak{S}) \tag{3.17}$$

where $\mathfrak{S}$ is all possible solutions. The objective function values from 100 optimization runs were collected to serve as an indication of this algorithm's performance. Figure 3.7 shows the interquartile range of this data.

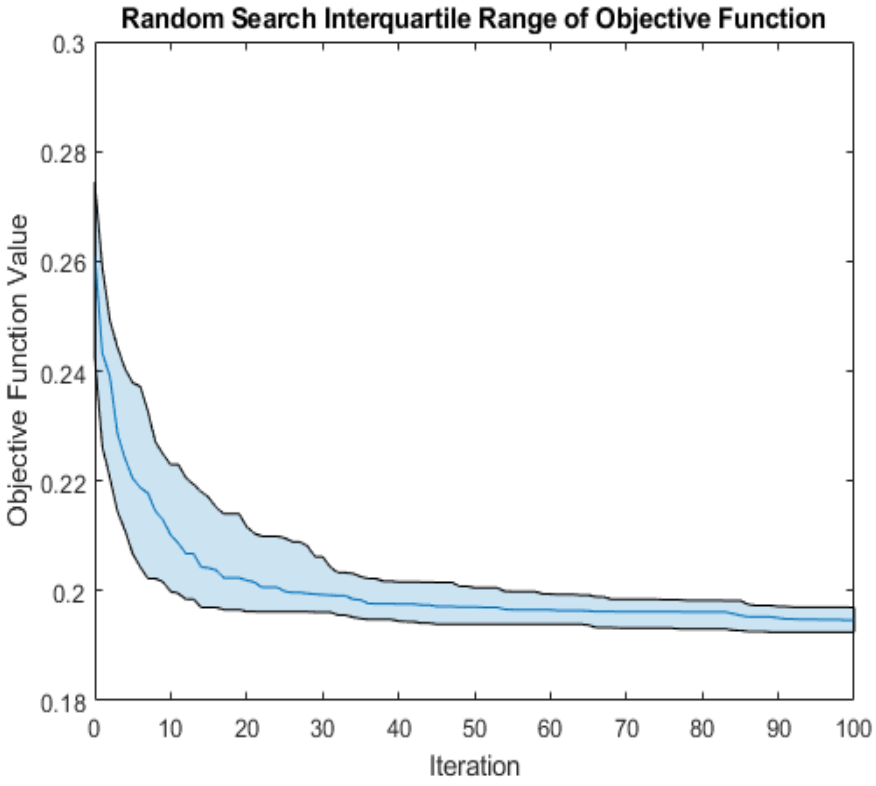

Figure 3.7: Random Search Interquartile Range

3.4.2 Genetic Algorithm

Genetic Algorithms have been employed to simulate natural selection and mating criteria. The idea of simulating learning with evolutionary processes was first proposed by Alan Turing. Essentially, given a population of candidate solutions, the solutions are first randomly mutated. Typically a parameter (Λ, f, d) is randomly selected and changed by a random value. Then the strongest solutions of the population have their attributes crossed over with one another.

Genetic algorithms are attractive because of their ability to generate extremely unique high-fitness solutions, that combine traits in constructive ways not able to be easily seen by humans. There are some considerable drawbacks to genetic algorithms, they often require a large number of function evaluations, and the number of function evaluations required increases exponentially with the dimensionality of the problem. This is not a problem with 1-dimensional grating, but more complex three-dimensional structures would have significant difficulties.

The specific Genetic Algorithm used in this comparison can be represented with the following heuristics[53]:

$$h_1 : \mathbf{s_n}(t+1) = (1 - \vec{m}) \odot \mathbf{s_n}(t) + \alpha \vec{m} \odot s_q \forall n \in [p_2 N, ..., N] \tag{3.18}$$

where where $\alpha = 1$ is the scale of the mutation,$p_2 = 0.125$ is the portion of the population protected from mutation,$\odot$is the Hadamard-Schur product, $\vec{m} = H(r_i - p_1)$, H is the component-wise Heaviside function,$p_1 = 0.25$ is the mutation percent. s_q is the uniform random variable: $s_q = U(-1, 1)$, and r_i is a uniform random variable: $r_i = U(0, 1)$. This is a mutation heuristic, which is then followed by a single point

cross over heuristic[48]:

$$h_2 : \mathbf{s_n}(t+1) = (1 - \vec{m}) \odot \vec{u} + m \odot \vec{v} \tag{3.19}$$

where $\vec{m} = H(i - z)$,$i = (1, 2, ..., D)^T$),$D = 3$ is the dimension of the problem, $z = U(1, D)$, $\vec{u}$ and $\vec{v}$ are the parents selected from a mating pool of size $p_3 N$, $p_3 = 1/3$ being the proportion of the population selected for mating. The objective function values from 50 optimization runs were collected to serve as an indication of this algorithm's performance. Figure 3.8 shows the interquartile range of this data.

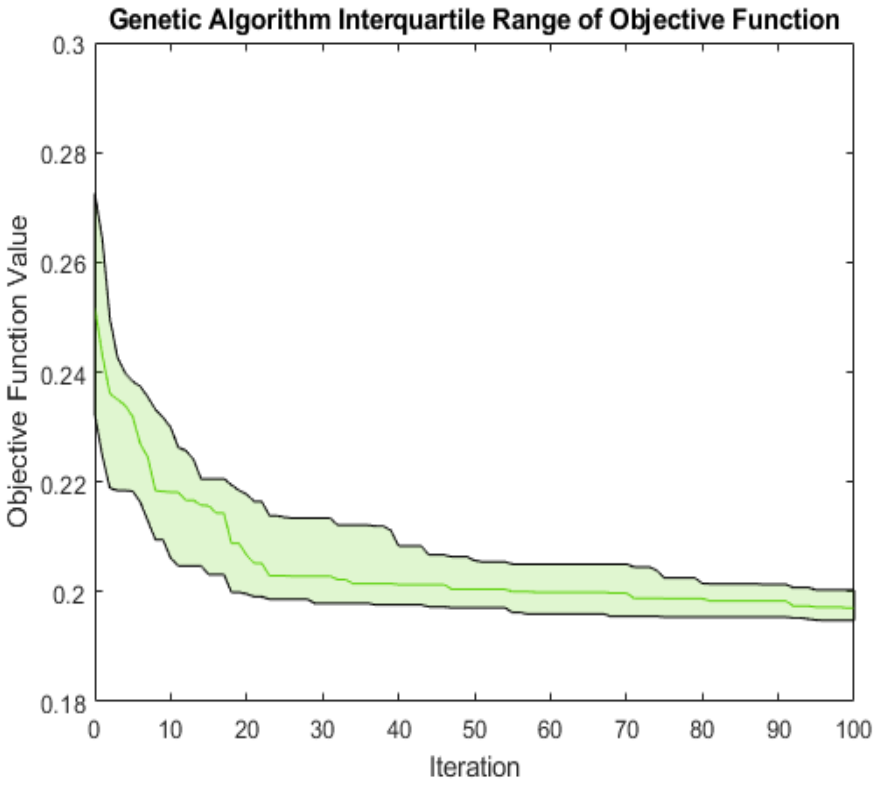

Figure 3.8: Genetic Algorithm Interquartile Range

3.4.3 Differential Evolution

Differential Evolution algorithms are extremely similar to Genetic Algorithms. The key difference is genetic algorithms were primarily conceived to operate on data represented as bitstrings, while Differential Evolution was designed to operate on real-valued numbers. However as seen in subsection 3.4.2, Genetic Algorithms can be modified to operate on real-valued numbers. The differential evolution algorithm explored in this study can be represented by the following heuristics[53]:

$$h_1 : \mathbf{s_n}(t+1) = \mathbf{s}_n(t) + F \cdot (\mathbf{s}_*(t) - \mathbf{s}_{z_1}(t)) + F \cdot \sum_{m=1}^{M} (\mathbf{s}_{z_{2m}}(t) - \mathbf{s}_{z_{2m+1}}(t)) \tag{3.20}$$

where $F = 1$ is the "strength" of the mutation, $M = 2$ is the number of Mutations, and $z_i \sim U(1, N)$ is a random member of the population of solutions. This is followed by a cross over heuristic:

$$h_2 : \mathbf{s_n}(t+1) = \mathbf{s_n}(\mathbf{i})(t) \leftarrow \mathbf{s_k}(\mathbf{i})(t),\ \mathbf{s_k}(\mathbf{i})(t) \leftarrow \mathbf{s_n}(\mathbf{i})(t) \tag{3.21}$$

where $\mathbf{s}_k$ is a random member of the population, and $\mathbf{i}$ is a randomly selected parameter of a solution. The objective function values from 50 optimization runs were collected to serve as an indication of this algorithm's performance. Figure 3.9 shows the interquartile range of this data.

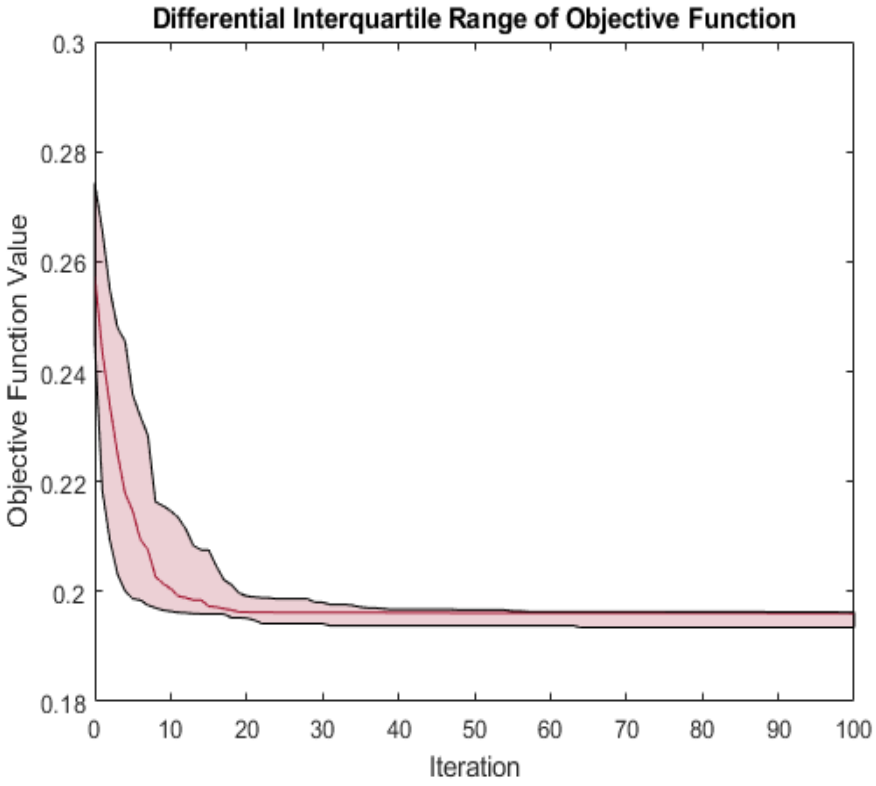

Figure 3.9: Differential Evolution Interquartile Range

3.4.4 Particle Swarm Optimization

Particle Swarm optimization (PSO) was originally intended to model avian social behavior [54], but was then re-adapted for optimization purposes. The particles use the information found by other particles to determine their velocity. The inertial particle swarm characteristic used in this study can be represented with the following heuristic:

$$h_1 : \mathbf{s_n}(t+1) = \mathbf{s_n}(t) + \vec{v_n}(t+1) \tag{3.22}$$

where

$$\vec{v_n}(t+1) = \omega_{PSO}\vec{v_n}(t) + \phi_{PSO1}\vec{r_1} \cdot (\mathbf{s}_{n,*}(t) - \mathbf{s}_n(t)) + \phi_{PSO2}\vec{r_2}(\mathbf{s}_*(t) - \mathbf{s}_n(t)) \tag{3.23}$$

and $\mathbf{s}_{n,*}$ is the best position that particle has found, $\omega_{PSO} = 1$, ϕ_{PSO1} is the strength of the particle's independent behavior, ϕ_{PSO2} is the strength of the particle's swarm behavior and $\vec{r_1}, \vec{r_2} = U(0,1)$. The objective function values from 50 optimization runs were collected to serve as an indication of this algorithm's performance. Figure 3.8 shows the interquartile range of this data.

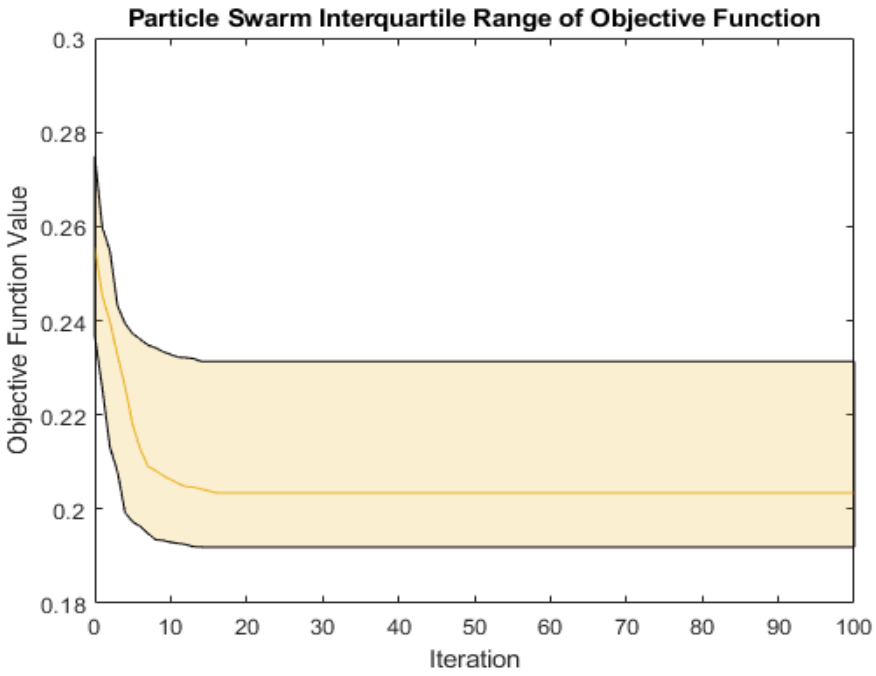

Figure 3.10: Particle Swarm Optimization Interquartile Range

The reason for the large interquartile range is due to premature convergence and a lack of exploration by the algorithm. This is due to the small population size of 8 and the parameters chosen. These parameters could be optimized through a similar process to the Hyper-heuristic search, called meta-optimization. This would almost certainly yield more efficient results than what is presented here. However, the focus of this study was Hyper-heuristic optimization, and controlling for the population allowed easy comparison between algorithms.

3.4.5 Firefly Optimization

The Firefly Algorithm FA is incredibly similar to particle swarm optimization, and critics have said the differences are negligible. The nature-inspired analogy fueling this algorithm is that a swarm of fireflies transmit information about the solution they have found in the form of light intensity, which dictates how the fireflies make their movements. The light intensity decays exponentially so fireflies farther away from light are less affected. This can be specifically represented with the following heuristic[55]:

$$h_1 : \mathbf{s_n}(t+1) = \mathbf{s_n}(t) + \alpha\vec{r} + \beta \sum_{k=1,=\neq n}^{N} H(-\Delta I_{n,k})\Delta\mathbf{s_{n,k}} \exp -\gamma|\mathbf{s_{n,k}}|^2 \tag{3.24}$$

where

$$\Delta I_{n.k} = F(\mathbf{s_k}(t)) - F(\mathbf{s_n}(t)) \tag{3.25}$$

and

$$\Delta\mathbf{s}_{n.k} = \mathbf{s_k}(t) - \mathbf{s_n}(t) \tag{3.26}$$

$\alpha = 1$,$\beta = 1$,$\gamma = 100$, and $\vec{r} = U(-0.5, 0.5)$. If instead $\gamma = 0$, the algorithm would almost exactly match a standard particle swarm optimization algorithm. The objective function values from 50 optimization runs were collected to serve as an indication of Firefly Optimization's performance. Figure 3.11 shows the interquartile range of this data.

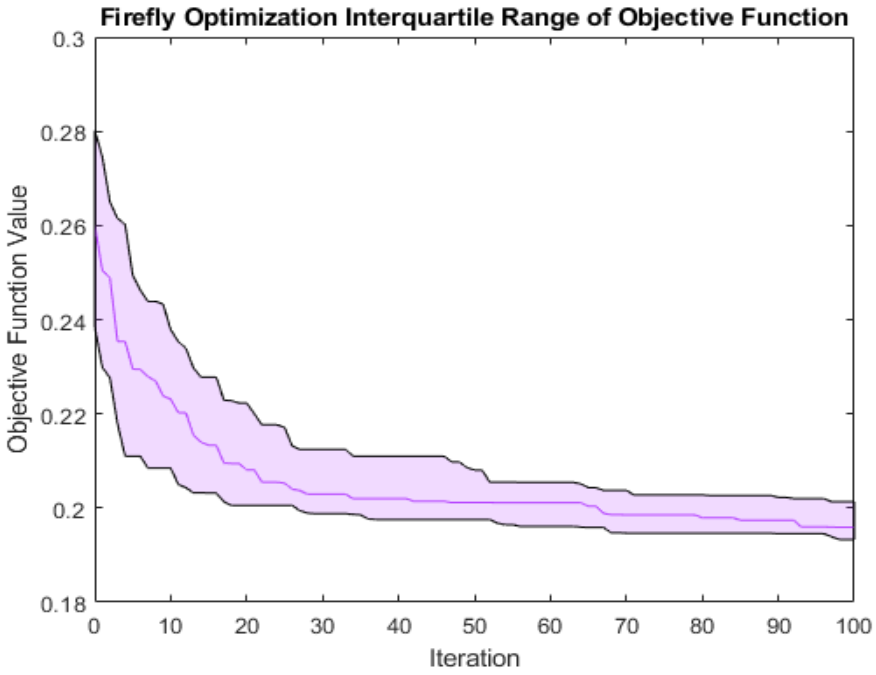

Figure 3.11: Firefly Optimization Interquartile Range

3.4.6 Overall Comparison

Overall the custom algorithm had much greater consistency, and convergence speed than all the other algorithms it was compared to. Figure 3.12 shows the 75th percentile of the optimization runs performed with each algorithm. Figure 3.12 shows the custom algorithm finds a better solution than every other algorithm 75% of the time. Figure 3.6 shows the extreme consistency in the new algorithm as well, there is a lower interquartile range at almost all iterations than the other algorithms. As discussed before, each of the comparison algorithms can have their defining parameters changed to improve their performance. The hyper-heuristic optimization essentially already tried different parameters of the comparison algorithms, and still found the new algorithm to be the best. Therefore, if each of the comparison algorithms were meta-optimized the result would probably be the same, albeit with the new algorithm having a less dramatic advantage.

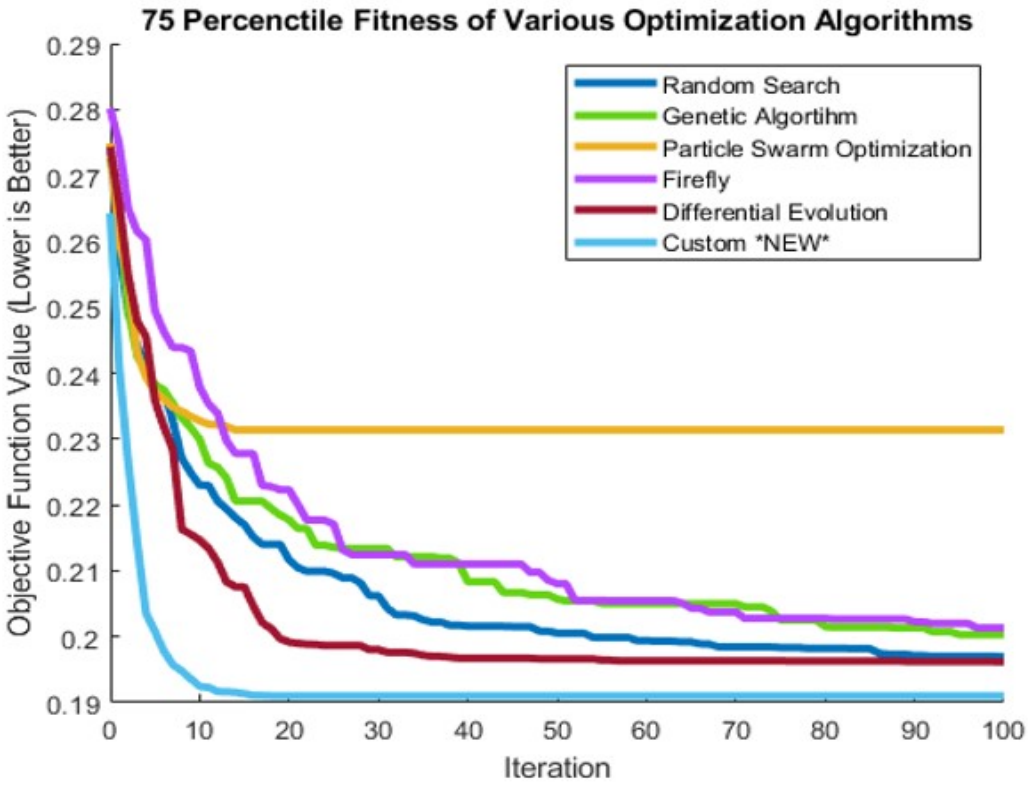

Figure 3.12: Metaheuristic Comparison

CHAPTER 4
OPTIMIZATION OF EMITTERS BASED ON MAXIMUM POWER AND EFFICIENCY

Often times when an emitter is optimized according to an ideal emittance spectrum problem, similar to subsection 3.2.1, it is serving as a proxy or for an actual desired system property. This is done because it is required that the problem be simplified because of the large computational time of calculating the actual system property. This chapter will shift focus away from these simplified problems and utilize the optimization algorithm generated in Chapter 3, to optimize the efficiency and power of a TPV system.

4.1 Efficiency and Power Model of a TPV System

Efficiency is particularly important for TPV systems. Solar photovoltaics typically have incident power on the order of ∼1kW, while TPV systems can have incident power on the order of ∼100kW. This means every photon that is not converted to electrical power results in excess heat raising the temperature of the cell. The efficiency of photovoltaic cells decreases as the temperature increase [56], and the components making solar cells can be damaged. For instance, the melting point of InSb is around 800K [57]. This requires extensive cooling infrastructure for these systems, and every increase in efficiency significantly reduces the amount of heat that needs to be removed.

Consider a TPV system composed of a Tungsten grating and a $In_{0.18}Ga_{0.82}Sb$ with a band gap of 0.56eV, the same system considered in subsection 3.2.1. This system can be modeled as as two infinite parallel plates. It is also assumed that

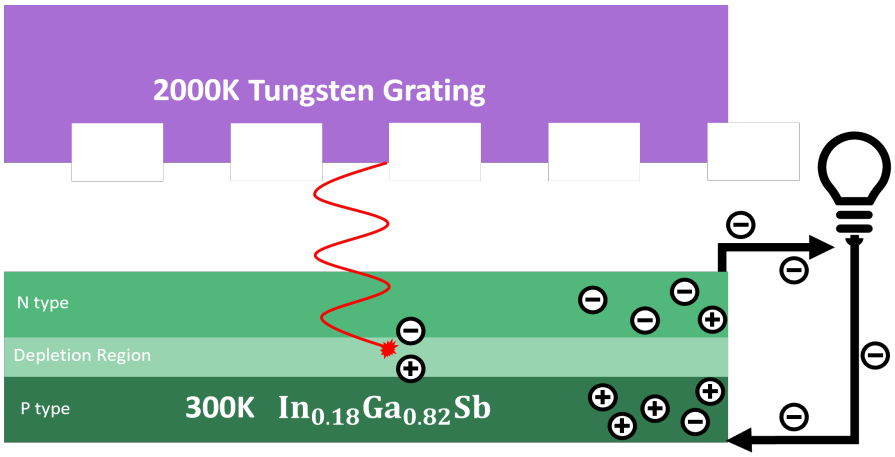

Figure 4.1: TPV System

the thermal radiation between the plates is far-field, meaning no evanescent waves contribute to the energy flux between the two plates. The flux for s polarized waves is[1]:

$$q" = \frac{1}{2\pi^3 c_0^2}\int_0^\infty \int_0^{\pi/2} \int_0^{\pi/2} [\Theta(\omega, T_2)] - \Theta(\omega, T_1)] \cdot [\frac{1}{1/\epsilon^s_{\omega,\theta,\phi,1} + 1/\epsilon^s_{\omega,\theta,\phi,2} - 1}]\omega^2 cos\theta sin\theta d\theta d\phi d\omega \tag{4.1}$$

and for p-polarized waves it is:

$$q" = \frac{1}{2\pi^3 c_0^2}\int_0^\infty \int_0^{\pi/2} \int_0^{\pi/2} [\Theta(\omega, T_2)] - \Theta(\omega, T_1)] [\frac{1}{1/\epsilon^p_{\omega,\theta,\phi,1} + 1/\epsilon^p_{\omega,\theta,\phi,2} - 1}]\omega^2 \cos\theta \sin\theta d\theta d\phi d\omega \tag{4.2}$$

where the mean energy of Planck's oscillator, $\Theta(\omega, T)$, is defined as [1]:

$$\Theta(\omega, T) = \frac{\hbar\omega}{\exp(\hbar\omega/k_B T) - 1} + \frac{\hbar\omega}{2} \tag{4.3}$$

1 and 2 are subscripts that denote the property for the emitter and the cell respectively such that T is the temperature, ϵ is the dielectric function[37], θ is the angle of

incidence from the normal direction, ϕ is the azimuthal angle, and ω is the frequency. Integrating over all possible frequencies is not feasible therefore a characteristic subset is used. This facilitates the introduction of ω_{max} and ω_{min}, which are the limits of the frequencies. For this particular model, limits of 0.4μm and 10μm with 200 logarithmically spaced frequencies were used with trapezoidal numerical integration. Similarly, the values were calculated every 5^o for the zenith and azimuthal angle for their trapezoidal numerical integration. This changes the flux equations to the following for s-polarized waves:

$$\begin{aligned} q" =& \frac{1}{2\pi^3 c_0^2} \int_{\omega_{min}}^{\omega_{max}} \int_0^{\pi/2} \int_0^{\pi/2} [\Theta(\omega, T_2)] - \Theta(\omega, T_1)] \\ & [\frac{1}{1/\epsilon^s_{\omega,\theta,\phi,1} + 1/\epsilon^s_{\omega,\theta,\phi,2} - 1}] \omega^2 cos\theta sin\theta d\theta d\phi d\omega \end{aligned} \tag{4.4}$$

and for p-polarized waves it is:

$$\begin{aligned} q" =& \frac{1}{2\pi^3 c_0^2} \int_{\omega_{\min}}^{\omega_{\max}} \int_0^{\pi/2} \int_0^{\pi/2} [\Theta(\omega, T_2)] - \Theta(\omega, T_1)] \\ & [\frac{1}{1/\epsilon^p_{\omega,\theta,\phi,1} + 1/\epsilon^p_{\omega,\theta,\phi,2} - 1}] \omega^2 \cos\theta \sin\theta d\theta d\phi d\omega \end{aligned} \tag{4.5}$$

The emittance values for the grating are obtained with RCWA by summing up the diffraction efficiency for 40 diffraction orders:

$$\epsilon = 1 - \sum_0^{40} \mathrm{DE}_j^r \tag{4.6}$$

It is worth noting again that RCWA calculations for azimuthal angles not equal to zero take significantly longer to calculate, due to conical diffraction effects. The emittance of the PV cell, $In_{0.18}Ga_{0.82}Sb$, was calculated with the Fresnel reflection coefficients [2]:

$$r_s = \frac{n_1 cos\theta_i - n_2 cos\theta_t}{n_1 cos\theta_i + n_2 cos\theta_t} \tag{4.7}$$

$$r_p = \frac{n_1 cos\theta_t - n_2 cos\theta_i}{n_1 cos\theta_t + n_2 cos\theta_i} \tag{4.8}$$

these equations can be manipulated to the following by solving for $cos\theta_t$:

$$r_s = \frac{n_1 cos\theta_i - n_2\sqrt{1 - (\frac{n_1}{n_2} sin\theta_i)^2}}{n_1 cos\theta_i + n_2\sqrt{1 - (\frac{n_1}{n_2} sin\theta_i)^2}} \tag{4.9}$$

$$r_p = \frac{n_1\sqrt{1 - (\frac{n_1}{n_2} sin\theta_i)^2} - n_2 cos\theta_i}{n_1\sqrt{1 - (\frac{n_1}{n_2} sin\theta_i)^2} + n_2 cos\theta_i} \tag{4.10}$$

where n_1 is the refractive index of the incident medium (vacuum), n_2 is the refractive index of the PV cell and θ_i is the zenith incident angle.

Once the radiative flux on the cell was determined, the current from photons was determined:

$$J_{ph} = \int_{\omega_g}^{\infty} \frac{e}{h\omega} q"(\omega) d\omega \tag{4.11}$$

where ω_g is the frequency associated with the band gap of the cell. This equation essentially assumes 100% internal quantum efficiency, that is every photon generates exactly one electron-hole pair. Then the diffusion current is assumed to be:

$$J_0 \approx J_{\text{Diffusion}} = e(\frac{N_i^2}{N_A}\sqrt{\frac{D_e}{\tau_e}} + (\frac{N_i^2}{N_D}\sqrt{\frac{D_h}{\tau_h}}) \tag{4.12}$$

which was calculated with the properties seen in Table 4.1. Then the Diffusion Current is used to find the dark current:

$$J_{dark} = J_0[exp(\frac{eV}{k_b T}) - 1] \tag{4.13}$$

.

Again, the power depends on the operating voltage. The maximum power gener-

Table 4.1: $In_{0.18}Ga_{0.82}Sb$ Cell Properties

Property	Value	Unit
N_A	10^{19}	cm^{-3}
N_D	10^{17}	cm^{-3}
N_i	10^{13}	cm^{-3}
D_e	125	$cm^2 s^{-1}$
D_h	31.3	$cm^2 s^{-1}$
τ_e	9.75	ns
τ_h	30.8	ns

ated is:

$$P_E = J_{ph} V_{oc} [1 - \frac{1}{\ln(J_{ph}/J_s)}][1 - \frac{\ln(\ln(J_{ph}/J_s))}{\ln(J_{ph}/J_s)}] \tag{4.14}$$

where

$$V_{oc} = \frac{k_b T}{e} \ln(J_{ph}/J_s + 1) \tag{4.15}$$

and $J_s = J_0$ is assumed. Then the efficiency, of the system is defined as:

$$\eta = \frac{P_E}{q"} \tag{4.16}$$

4.2 Optimizing Efficiency and Power

The above model allows for 2 new optimization problems, one for efficiency:

$$\begin{aligned} \max_{\Lambda,f,d} F_{\text{eff}}(\boldsymbol{s}) &= \eta(\boldsymbol{s}) \\ \text{Subject To: } 0.3\mu m \leq \Lambda &\leq 2.0\mu m \\ 0.1 \leq f &\leq 0.9 \\ 0.3\mu m \leq d &\leq 2.0\mu m \end{aligned} \tag{4.17}$$

and one for maximum power output:

$$\begin{aligned} \max_{\Lambda,f,d} F_{\text{power}}(\boldsymbol{s}) &= P_E(\boldsymbol{s}) \\ \text{Subject To: } 0.3\mu m \leq \Lambda &\leq 2.0\mu m \\ 0.1 \leq f &\leq 0.9 \\ 0.3\mu m \leq d &\leq 2.0\mu m \end{aligned} \tag{4.18}$$

Both of these problems were then optimized using the new algorithm created and defined in subsection 3.2.2 and section 3.3. The optimization problem the algorithm was originally designed for is different from and , so this served as a test of the algorithm's application to similar optimization problems. Each problem was optimized using a population size of 8, for 100 iterations. This optimization procedure was performed 5 times, to see the variability in the convergence of the algorithm, as more optimization runs were computationally infeasible.

4.2.1 Optimization Results

Table 4.2: Optimized Gratings for Different Objective Functions

Function	$F_1(\boldsymbol{s})$	$\text{F}_{\text{power}}(\boldsymbol{s})$	$\text{F}_{\text{eff}}(\boldsymbol{s})$
$\Lambda[\mu\text{m}]$	1.11	1.11	1.11
f	0.14	0.1	0.1
$d[\mu\text{m}]$	2	2	2
η	26.90	27.06	27.06
$P_E[\text{kWm}^{-2}]$	71.16	71.91	71.91
Emitter #	1	2	2

All three emitters optimized for different properties were extremely similar; in fact, the optimization for power and efficiency actually converged on the same grating. This is surprising as it was expected that maximum power and efficiency would be Pareto-optimal. Also, all of the emitters converged to the boundary of the search space. This means that the original set of original possible solutions is not com-

prehensive and expansion of this search space would almost certainly yield a better emitter. However, the extremely similar nature between these two emitters shows that non-conical diffraction and normal incidence optical properties serve as an excellent proxy or surrogate loss function for power and efficiency optimization. The optimized emitters were given numbers to identify them. The emitter optimized for the normal incident problem is designated as "1" and the emitter optimized for power and efficiency is designated as 2.

4.3 Optical Properties of the Emitters

The similarities of the emitters extends to their optical characteristics as well. The hemispherical and normal emittance for each emitter is depicted in Figure 4.2 and Figure 4.3. The TE and TM waves almost seem to mirror each other, for example at short wavelengths ($0.4 - 1.3\mu$m) emitter 1 has higher TM emittance and lower TE emittance than at longer wavelength just above the band gap, TE has a higher emittance characterized by 2 distinct peaks. Similar behavior is observed in emitter 2 yet the large peaks seen just near the bandgap are red-shifted slightly. Both emitters have a constant low emittance of about 0.1 at wavelengths longer than the bandgap, albeit emitter 2 has a slightly lower emittance in this region. The hemispherical emittance is of course not as dramatic and is essentially identical between emitters 1 and 2.

Full contour plots at $2\mu m$ were produced of each emitter to provide insight into why $F_1(\boldsymbol{s})$ is a good surrogate for efficiency and power optimization. A wavelength of $2\mu m$ was chosen based on the geometric parameter values of the gratings. $2\mu m$ Both emitters actually have their largest emittance values resulting from a zenith angle of about 50^o. This was true for most wavelengths and not just the shown values at $2\mu m$. Both emitters also have a sort of "dark zone" at higher zenith angles in between

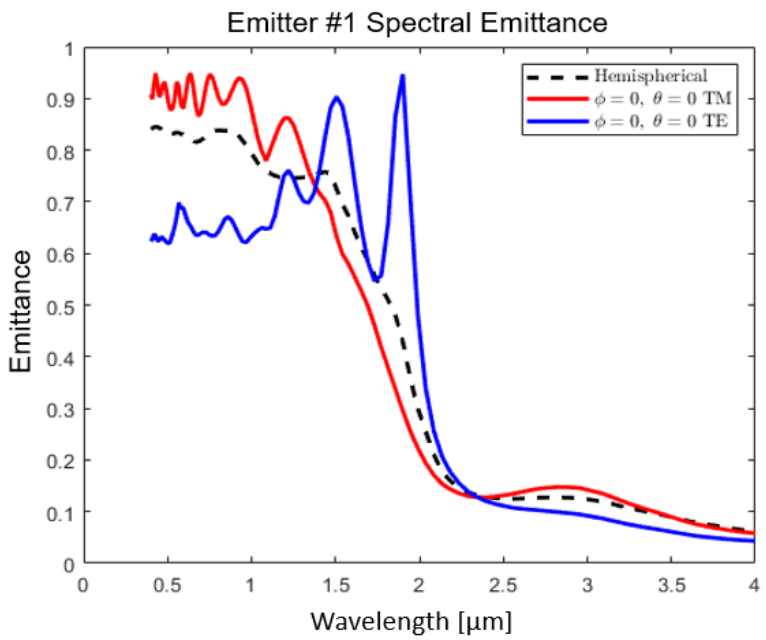

Figure 4.2: Emitter 1 Optical Properties

azimuthal angles of 30^o and 60^o. It is also interesting that both optimization results are similar despite $F_1(\boldsymbol{s})$ having no optical information about the cell or operating conditions of the TPV system, which shows that the normal spectral emittance is a good starting point for TPV system optimization.

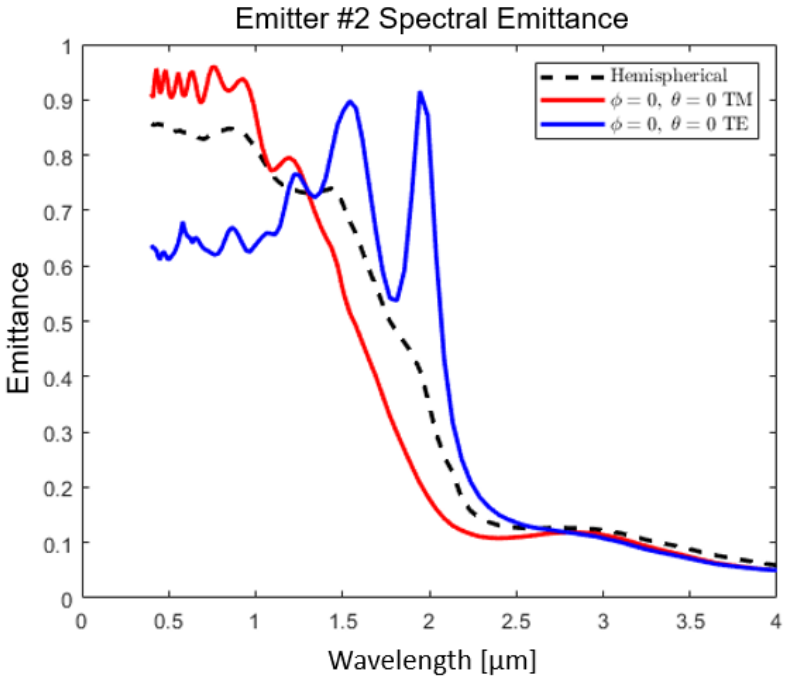

Figure 4.3: Emitter 2 Optical Properties

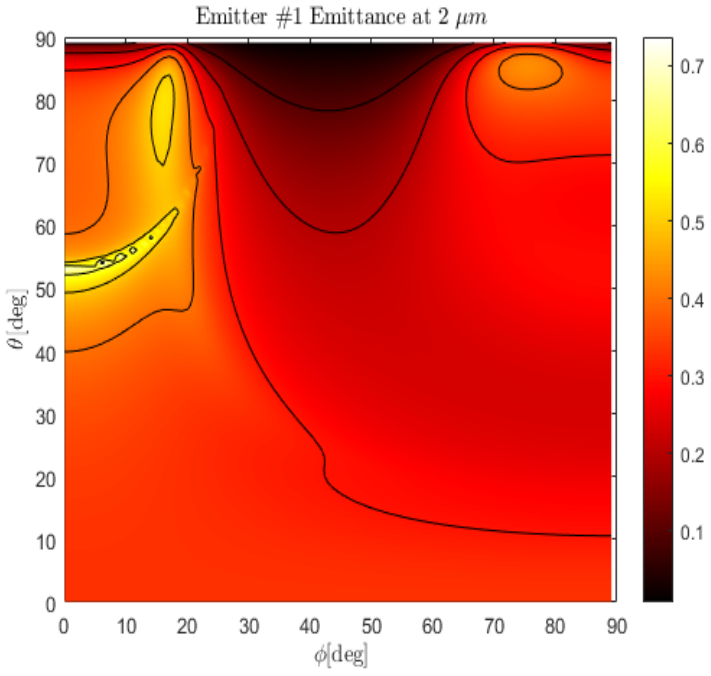

Figure 4.4: Emitter 1 Emittance Contour at 2 μm

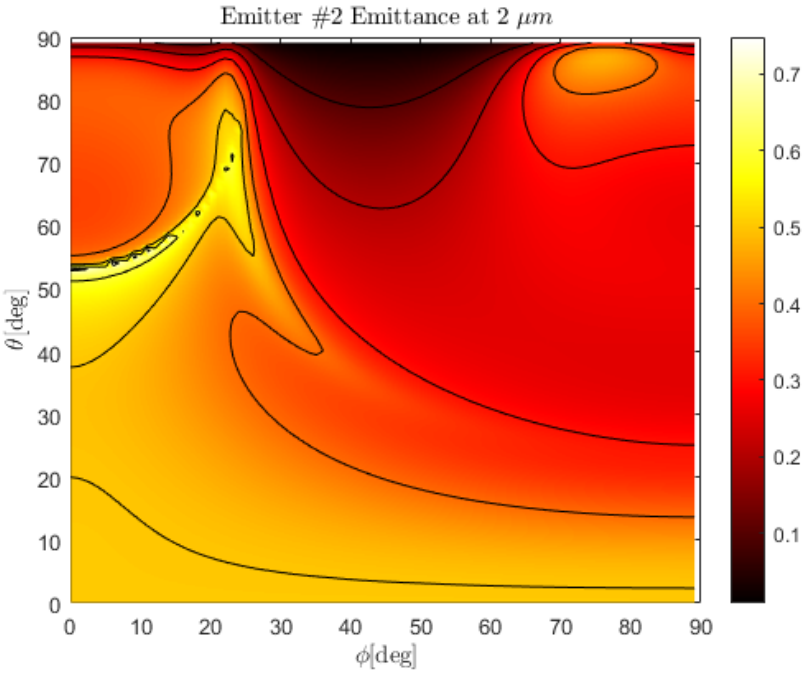

Figure 4.5: Emitter 2 Emittance Contour at 2 μm

CHAPTER 5
CONCLUSION

Thermophotovoltaics remains a promising technology with a growing range of applications and their utility will increase as more unique and efficient power systems are needed. Binary gratings utilized as selective emitters are just one way the efficiency of TPV systems can be improved. Selective emitters can be used in conjunction with other efficiency improving technologies (e.g. multi-junction photovoltaic cells, anti-reflection coatings, and back reflectors). This study primarily showed how to create efficient optimizers for the design of binary gratings. Highly efficient optimization algorithms for designing emitters are paramount for selective emitter utilization and adoption. This will be particularly true when the geometric parameters of the emitters are being optimized alongside system configurations. This study showed how Hyper-heuristic techniques can be employed to facilitate the creation of these highly efficient optimization algorithms. This creation of new algorithms was facilitated with fully connected neural nets serving as RCWA surrogates for the calculation of optical properties.

An investigation into the full efficiency and power output of a TPV system showed that simplified surrogate objective functions based on normal spectral emittance properties are good baseline optimizers when compared to optimizing for efficiency and power directly. System efficiency and power are several orders of magnitude more computationally expensive than the normal spectral emittance, increasing the speed at which an ideal binary grating can be found. Better-designed surrogate objective functions could serve as even better initial optimization problems. For instance, a surrogate function involving a normal incidence spectrum where the wavelengths are

weighted based on their difference from the bandgap could serve to better mimic the thermalization processes captured with efficiency calculations. These optimization techniques could also be explored for TPV systems taking advantage of evanescent waves and photon tunneling effects, a phenomena that has been shown to significantly increase the efficiency of TPV systems. Fabrication is the major barrier for further development and utilization of these near-field thermophotovoltaics.

There still remain key challenges and problems that need to be addressed before the widespread adoption of thermophotovoltaics. TPV application has been mostly relegated to low-power systems due to their efficiency and high fabrication cost. Nano-materials particularly one-dimensional gratings, serve as a tool to increase the efficiency of these systems and will pave the way for more high-powered macroscale TPV applications. Yet the fabrication of these materials is a roadblock to their adoption. This is where the simplicity of one-dimensional binary gratings becomes useful compared to other sub-wavelength structures.

REFERENCES

[1] Z. M. Zhang, *Nano/Microscale Heat Transfer 2nd ed.* Springer, Cham, Switzerland, 2020.

[2] M. F. Modest, *Radiative heat transfer*. Academic Press, 2013.

[3] W. Cai and V. M. Shalaev, *Optical metamaterials: fundamentals and applications*. Springer, 2016.

[4] R. Z. Zhang and Z. M. Zhang, "Negative refraction and self-collimation in the far infrared with aligned carbon nanotube films," *Journal of Quantitative Spectroscopy and Radiative Transfer*, vol. 158, pp. 91–100, 2015.

[5] R. Z. Zhang and Z. M. Zhang, "Tunable positive and negative refraction of infrared radiation in graphene-dielectric multilayers," *Applied Physics Letters*, vol. 107, no. 19, p. 191 112, 2015.

[6] J. I. Watjen, X. L. Liu, B. Zhao, and Z. M. Zhang, "A computational simulation of using tungsten gratings in near-field thermophotovoltaic devices," *Journal of Heat Transfer*, vol. 139, no. 5, 2017.

[7] N. Nguyen-Huu, Y.-B. Chen, and Y.-L. Lo, "Development of a polarization-insensitive thermophotovoltaic emitter with a binary grating," *Optics Express*, vol. 20, no. 6, p. 5882, 2012.

[8] X. Zhang and Z. Liu, "Superlenses to overcome the diffraction limit," *Nature Materials*, vol. 7, no. 6, pp. 435–441, 2008.

[9] W. Cai, U. K. Chettiar, A. V. Kildishev, and V. M. Shalaev, "Optical cloaking with metamaterials," *Nature Photonics*, vol. 1, no. 4, pp. 224–227, 2007.

[10] A. Sakurai, B. Zhao, and Z. M. Zhang, "Effect of polarization on dual-band infrared metamaterial emitters or absorbers," *Journal of Quantitative Spectroscopy and Radiative Transfer*, vol. 158, pp. 111–118, 2015.

[11] X. Wu, C. Fu, and Z. M. Zhang, "Chiral response of a twisted bilayer of hexagonal boron nitride," *Optics Communications*, vol. 452, pp. 124–129, 2019.

[12] L. E. Mackenzie and P. Stachelek, "The twists and turns of chiral chemistry," *Nature Chemistry*, vol. 13, no. 6, pp. 521–522, 2021.

[13] B. Woodcroft and J. G. Greenwood, *The pneumatics of Hero of Alexandria: From the ancient greek*. Taylor Walton and Maberly, 1851.

[14] P. Rappaport, "The photovoltaic effect and its utilization," *Solar Energy*, vol. 3, no. 3, p. 50, 1959.

[15] A. R. Zanatta, "Revisiting the optical bandgap of semiconductors and the proposal of a unified methodology to its determination," *Scientific Reports*, vol. 9, no. 1, 2019.

[16] D. A. Neamen and D. Biswas, *Semiconductor Physics and Devices*. McGraw Hill Education (India), 2020.

[17] E. Rosencher, B. Vinter, and P. G. Piva, *Optoelectronics*. Cambridge University Press, 2002.

[18] J. I. Pankove, *Optical processes in semiconductors*. Dover Publications, Inc., 2018.

[19] L. I. Berger, *Semiconductor materials*. CRC Press, 2020.

[20] R. Rousina, C. Halpin, and J. B. Webb, "Growth and characterization of in1xgaxsb by metalorganic magnetron sputtering," *Journal of Applied Physics*, vol. 68, no. 5, pp. 2181–2186, 1990.

[21] V. P. Singh, R. Singh, and K. E. Sampson, "Thin-film solar cells based on nanostructured cds, cis, cdte and cu2s," *Nanostructured Materials for Solar Energy Conversion*, pp. 167–190, 2006.

[22] S. Miao, S. G. Hickey, B. Rellinghaus, C. Waurisch, and A. Eychmüller, "Synthesis and characterization of cadmium phosphide quantum dots emitting in the visible red to near-infrared," *Journal of the American Chemical Society*, vol. 132, no. 16, pp. 5613–5615, 2010.

[23] R. Gillen and J. Robertson, "Band structure calculations of cualo2, cugao2, cuino2, and cucro2 by screened exchange," *Physical Review B*, vol. 84, no. 3, 2011.

[24] T. Omata, H. Nagatani, I. Suzuki, M. Kita, H. Yanagi, and N. Ohashi, "Wurtzite cugao2: A new direct and narrow band gap oxide semiconductor applicable as a solar cell absorber," *ChemInform*, vol. 45, no. 26, 2014.

[25] R. F. Pierret, *Semiconductor device fundamentals*. Pearson/Education, 2008.

[26] T. J. Bright, X. L. Liu, and Z. M. Zhang, "Energy streamlines in near-field radiative heat transfer between hyperbolic metamaterials," *Optics Express*, vol. 22, no. S4, 2014.

[27] X. Wang, R. Liang, P. Fisher, W. Chan, and J. Xu, "Radioisotope thermophotovoltaic generator design methods and performance estimates for space missions," *Journal of Propulsion and Power*, vol. 36, no. 4, pp. 593–603, 2020.

[28] A. Lenert *et al.*, "A nanophotonic solar thermophotovoltaic device," *Nature Nanotechnology*, vol. 9, no. 2, pp. 126–130, 2014.

[29] A. K. Hyder, *Spacecraft Power Technologies*. Imperial College Press, 2003.

[30] S. Basu, Y.-B. Chen, and Z. M. Zhang, "Microscale radiation in thermophotovoltaic devices—a review," *International Journal of Energy Research*, vol. 31, no. 6-7, pp. 689–716, 2007.

[31] R. Sakakibara *et al.*, "Practical emitters for thermophotovoltaics: A review," *Journal of Photonics for Energy*, vol. 9, no. 03, p. 1, 2019.

[32] M. Laroche *et al.*, "Highly directional radiation generated by a tungsten thermal source," *Optics Letters*, vol. 30, no. 19, p. 2623, 2005.

[33] Y.-B. Chen and Z. Zhang, "Design of tungsten complex gratings for thermophotovoltaic radiators," *Optics Communications*, Sep. 2006.

[34] I. Celanovic, N. Jovanovic, and J. Kassakian, "Two-dimensional tungsten photonic crystals as selective thermal emitters," *Applied Physics Letters*, vol. 92, no. 19, p. 193 101, 2008.

[35] E. Lassner and W.-D. Schubert, *Tungsten: Properties, chemistry, technology of the elements, alloys and chemical compounds*. Kluwer Academic, 1999.

[36] A. Narayanaswamy and G. Chen, "Thermal emission control with one-dimensional metallodielectric photonic crystals," *Physical Review B*, vol. 70, no. 12, 2004.

[37] E. D. Palik, *Handbook of Optical Constants of Solids II*. Academic Press, 1998.

[38] J. Liu, S. J. Zhang, and Y. S. Chen, "Rigorous electromagnetic modeling of radiative interactions with microstructures using the finite volume time-domain method," *International Journal of Thermophysics*, vol. 25, no. 4, pp. 1281–1297, 2004.

[39] P. Lalanne and D. Lemercier-lalanne, "On the effective medium theory of subwavelength periodic structures," *Journal of Modern Optics*, vol. 43, no. 10, pp. 2063–2085, 1996.

[40] M. G. Moharam and T. K. Gaylord, "Rigorous coupled-wave analysis of planar-grating diffraction," *Journal of the Optical Society of America*, vol. 71, no. 7, p. 811, 1981.

[41] M. G. Moharam, T. K. Gaylord, E. B. Grann, and D. A. Pommet, "Formulation for stable and efficient implementation of the rigorous coupled-wave analysis of binary gratings," *Journal of the Optical Society of America A*, vol. 12, no. 5, p. 1068, 1995.

[42] B. Zhao, L. Wang, Y. Shuai, and Z. M. Zhang, "Thermophotovoltaic emitters based on a two-dimensional grating/thin-film nanostructure," *International Journal of Heat and Mass Transfer*, vol. 67, pp. 637–645, 2013.

[43] R. Hu *et al.*, "Machine learning-optimized tamm emitter for high-performance thermophotovoltaic system with detailed balance analysis," *Nano Energy*, vol. 72, p. 104 687, 2020.

[44] D. P. Kingma and J. Ba, *Adam: A method for stochastic optimization*, 2014.

[45] S. Shan, B. Chen, and C. Shou, "Parametric characteristics and optimization of a near-field thermophotovoltaic system considering cooling consumption," *Solar Energy*, vol. 224, pp. 629–636, 2021.

[46] M. M. Gamel *et al.*, "Multi-dimensional optimization of in0.53ga0.47as thermophotovoltaic cell using real coded genetic algorithm," *Scientific Reports*, vol. 11, no. 1, 2021.

[47] Y. Khorrami and D. Fathi, "Broadband thermophotovoltaic emitter using magnetic polaritons based on optimized one- and two-dimensional multilayer structures," *Journal of the Optical Society of America B*, vol. 36, no. 3, p. 662, 2019.

[48] J. M. Cruz-Duarte, I. Amaya, J. C. Ortiz-Bayliss, H. Terashima-Marín, and Y. Shi, "Customhys: Customising optimisation metaheuristics via hyper-heuristic search," *SoftwareX*, vol. 12, p. 100 628, 2020.

[49] Y. Lu, M. H. Cho, Y. Lee, and J. Y. Rhee, "Polarization-independent extraordinary optical transmission in one-dimensional metallic gratings with broad slits," *Applied Physics Letters*, vol. 93, no. 6, p. 061 102, 2008.

[50] B. J. Lee, Y. Chen, and Z. Zhang, "Transmission enhancement through nanoscale metallic slit arrays from the visible to mid-infrared," *Journal of Computational and Theoretical Nanoscience*, vol. 5, pp. 201–213, Feb. 2008.

[51] O. I. Abiodun, A. Jantan, A. E. Omolara, K. V. Dada, N. A. Mohamed, and H. Arshad, "State-of-the-art in artificial neural network applications: A survey," *Heliyon*, vol. 4, no. 11, 2018.

[52] K. Clark, M.-T. Luong, C. D. Manning, and Q. Le, "Semi-supervised sequence modeling with cross-view training," *Proceedings of the 2018 Conference on Empirical Methods in Natural Language Processing*, 2018.

[53] J. M. Cruz-Duarte, I. Amaya, J. C. Ortiz-Bayliss, S. E. Conant-Pablos, and H. Terashima-Marin, "A primary study on hyper-heuristics to customise metaheuristics for continuous optimisation," *2020 IEEE Congress on Evolutionary Computation (CEC)*, 2020.

[54] J. Kennedy and R. Eberhart, "Particle swarm optimization," *Proceedings of ICNN'95 - International Conference on Neural Networks*,

[55] X.-S. Yang, *Nature-inspired metaheuristic algorithms*. Luniver Press, 2010.

[56] P. Singh and N. Ravindra, "Temperature dependence of solar cell performance—an analysis," *Solar Energy Materials and Solar Cells*, vol. 101, pp. 36–45, 2012.

[57] L. Zhang, N. Li, Q. Meng, J. Zhang, and Z. Lei, "Study on thermal effects of insb infrared focal plane arrays irradiated by pulsed laser," *Optical and Quantum Electronics*, vol. 50, no. 5, 2018.